



# From thin air to pure water: Enhancing atmospheric water harvesting with molecular dynamics simulations of pristine and porous zirconium-based MOF-801

Seyed Faridedin Rafie<sup>a</sup>, Nidal Abu-Zahra<sup>a,\*</sup>, Roozbeh Sabetvand<sup>b</sup>

<sup>a</sup> Materials Science and Engineering Department, University of Wisconsin-Milwaukee, Milwaukee, WI 53211, USA

<sup>b</sup> Department of Energy Engineering and Physics, Faculty of Condensed Matter Physics, Amirkabir University of Technology, Tehran, Iran

## ARTICLE INFO

### Keywords:

Adsorption  
AWH  
MOF  
Water adsorption  
Desorption  
MD simulations

## ABSTRACT

Water scarcity affects a substantial portion of the global population, necessitating innovative solutions for sustainable water management. This study investigates the use of Metal-Organic Frameworks (MOFs), specifically Zr-MOF-801, for atmospheric water harvesting (AWH) through molecular dynamics (MD) simulations. Employing the Universal Force Field (UFF) and DREIDING Force Field, simulations model atom interactions using Lennard-Jones potential parameters ( $\epsilon$ ,  $\sigma$ ) and harmonic oscillator models for bonded interactions. Simulation phases encompassed rigorous minimization, equilibration under NVT conditions, and adsorption under NVE conditions to analyze moisture uptake and water release. Several critical parameters such as potential energy, kinetic energy, interaction energy, enthalpy, bond energy, mean square displacement (MSD), and root mean square deviation (RMSD) were calculated to analyze the adsorption and desorption phenomena. Subsequent 2nd cycle of adsorption phases investigated, evaluating material durability and reusability in AWH contexts. During the first adsorption cycle, simulations reveal significant variations in water adsorption capacity. Pristine MOF-801 and samples with 1 %, 2 %, 3 %, 5 %, and 10 % porosity adsorbed 3771, 3355, 3790, 3630, 3773, and 3716 water atoms, respectively. The optimal balance between adsorbent atom reduction and increased adsorption sites was observed at 2 % porosity, enhancing adsorption efficiency while maintaining structural stability. Analysis of potential energy indicates improved stability with increasing porosity in the cases of pristine MOF-801 at -12933.3 kcal/mol and MOF-801 at 10 % porosity at -32971.8 kcal/mol. This trend highlights porosity's role in reducing structural degradation during adsorption. Additionally, interaction energies between MOF-801 and water molecules ranged from -964.818 kcal/mol (pristine) to -1079.38 kcal/mol (10 % porosity), underscoring the influence of porosity on adsorption strength. The desorption phase demonstrates that higher porosity facilitates faster water release under elevated temperatures, with MOF-801 at 2 % porosity exhibiting optimal performance. In the second adsorption cycle, the impact of porosity became evident, with pristine MOF-801 exhibiting a 21.3 % reduction in adsorption efficiency compared to the first cycle. However, samples with 2 % and 3 % porosity experienced only slight reductions in adsorption efficiency, with decreases of 3.06 % and 0.11 %, respectively. This highlights their enhanced durability and potential for reuse.

## 1. Introduction

Water scarcity affects over 40 % of the global population, with 700 million lacking clean drinking water [1]. Despite 71 % of Earth's surface being water, only 3 % is freshwater, and just 0.06 % is easily accessible [2]. Most freshwater is locked in glaciers and groundwater, and around 50 % of wastewater is discharged untreated [1]. Over-extraction, poor management, and contamination contribute to desertification,

migration, and conflict, while population growth and urbanization increase demand [3–5]. By 2050, the global population will reach 10.2 billion, intensifying water withdrawals [2,5]. Agriculture consumes 70 % of freshwater [4,6], and groundwater, crucial for agriculture, constitutes 99 % of accessible freshwater [2,7]. Climate change worsens water scarcity by altering hydrological cycles [8–10]. Solutions include efficient water use, technological innovations, and policy reforms, such as advances in sustainable irrigation, smart water management [11,12],

\* Corresponding author.

E-mail address: [nidal@uwm.edu](mailto:nidal@uwm.edu) (N. Abu-Zahra).

adsorbents [13,14], nano-membranes [15,16], photocatalysis, and desalination [17–19].

Atmospheric water, comprising ~10 % of freshwater, offers a sustainable supply regardless of geography [20,21]. AWH is a decentralized strategy for rural areas, overcoming local humidity constraints [20]. Traditional methods, like cooling air below the dew point, incur high energy costs [22]. Moisture-harvesting materials, such as sorbents, allow water extraction even in low humidity [23]. AWH methods include fog and dew collection, vapor concentration, and sorption-based techniques, with sorption-based AWH (SAWH) standing out for its efficiency in arid regions [24,25]. SAWH uses sorbents that capture and release water via physisorption, driven by van der Waals forces for rapid adsorption/desorption [26]. Effective sorbents require high capacity, stability, and surface area [27,28]. In SAWH, adsorbents are classified into traditional chemical sorbents, hydrogels, and Metal-Organic Frameworks (MOFs). Chemical sorbents like hygroscopic salts have high water affinity but stability issues, while physical sorbents like silica gels and zeolites have lower capacities. Zeolite 13X modified with carbon black adsorbs 0.31 g/g of water under solar irradiation [29], while silica gel yields 800 mL of water per kilogram daily under specific conditions [30]. Hydrogels offer significant storage capacity but require improvements in stability and kinetics, with macroporous hydrogels achieving sorption capacities of 433.72 % at 98 % RH [31]. MOFs, with high porosity and customizable structures, are promising due to their superior thermal stability. Various MOFs have proven effective for adsorption in different applications, as demonstrated by Alsuhaihani et al. in their study on Cr(VI) removal. Notably, the NH<sub>2</sub>-Ag-MOF@CSC composite sponge achieves a high adsorption capacity of 382.6 mg/g and maintains stability across multiple cycles. Its performance is enhanced by mechanisms such as  $\pi$ - $\pi$  interactions, hydrogen bonding, electrostatic interactions, and pore filling. The adsorption follows Langmuir isotherm and pseudo-second-order kinetic models, indicating monolayer chemisorption with an energy of 22.42 kJ/mol [32]. However based on application choices can be different. Zirconium-based MOFs like MOF-801 exhibit high water adsorption at low humidity, with MOF-801 capable of harvesting 2.8 L of water per kilogram daily at 20 % RH using sunlight [33–35]. Advances such as surface functionalization, doping, and integration into membranes have further enhanced their performance [25,36,37]. Reusability and stability after multiple cycles are crucial in adsorption applications. For example, in a study by Nassef et al., the Ag-MOF/chitosan composite sponge (Ag-MOF/CSC) retained its chemical composition and adsorption capacity after six cycles, with consistent XRD and XPS results [38]. In the current study, a second cycle of adsorption was simulated to further investigate these properties.

Molecular simulation has become an essential tool for elucidating sorption mechanisms, offering molecular-level insights into interactions and structural dynamics. In order to study the behavior and interactions of materials at the atomic or molecular level, molecular simulation techniques—such as Monte Carlo (MC) modeling, MD simulations, and quantum mechanical calculations—have become indispensable [39]. By enabling the thorough modeling of intricate systems, these techniques shed light on the mechanisms underlying the processes involved in pollutant removal. Materials for contaminant adsorption, degradation, or filtration can be designed and optimized more easily thanks to MD simulations, which, for instance, can capture the dynamic behavior of molecules in a variety of environments [40]. Quantum mechanical computations provide profound insights into electronic interactions and reaction pathways, while Monte Carlo simulations are frequently used to forecast thermodynamic properties and equilibrium states [41,42]. The ability to forecast material performance under different conditions, optimize material properties for increased efficiency, and eliminate the need for extensive experimental trials are just a few of the many benefits of these methods in pollutant removal that speed up the development of sustainable and affordable environmental solutions. MD simulations, in particular, predict atomic and molecular movements over time, enabling

the discovery and optimization of novel adsorbents in controlled environments [43,44]. These simulations provide critical data on adsorption dynamics, interactions, and transport properties, enhancing our understanding of adsorption processes [45]. Firouzjaei et al. used MD simulations to study dye adsorption by a graphene oxide-copper-MOF (GO-Cu-MOF) nanocomposite, finding adsorption energies of -323 kCal/mol and -119 kCal/mol for GO-Cu-MOF and Cu-MOF, respectively, in agreement with experimental data [46]. Similarly, Rafie et al. employed MD to validate experimental findings for Ni<sub>x</sub>Co<sub>1-x</sub>Fe<sub>2</sub>O<sub>4</sub>, showing that Ni<sub>x</sub>Co<sub>1-x</sub>Fe<sub>2</sub>O<sub>4</sub> ( $x = 0.75$ ) was most effective in removing Zn(II), supported by analyses of interaction energies, mean square displacement (MSD), and root mean square deviation (RMSD) [47]. Despite their advantages, MD simulations are limited to short timescales (typically tens of nanoseconds) [48]. Comparing simulation results with long-term experimental data helps bridge this gap, offering a more comprehensive understanding of adsorption and desorption behaviors. Using computational simulations is of interest to researchers working on AWH. In a study conducted by Li et al., MOF-303 was evaluated for AWH in polluted environments using GCMC and DFT methods. MOF-303 demonstrated strong water adsorption (0.50 g/g at 298 K, 3000 Pa) and high SO<sub>2</sub> affinity (0.40 g/g), with minimal NO and NO<sub>2</sub> uptake. In mixed systems, water adsorption dominated, highlighting MOF-303's potential for AWH and air quality control in polluted settings [49]. In another study conducted by K. Sibie et al., water absorption using anhydrous salts (CuCl<sub>2</sub>, CuSO<sub>4</sub>, MgSO<sub>4</sub>) was modeled and simulated, with results compared to experimental data [50]. Sensitivity analysis was used to examine the effects of porosity, thickness, and uniformity on absorption efficiency. Copper chloride showed the highest saturation (88.75 kg L/kg S) at 15 % RH, while copper sulfate and magnesium sulfate reached 81.80 kg L/kg S and 76.83 kg L/kg S at 35 % RH. In dynamic RH mode, copper chloride reached 98.61 kg L/kg S. The analysis revealed that thinner salt sheets and higher porosity increased water adsorption.

This study introduces a novel investigation into the optimization of AWH using MD simulations to systematically evaluate the performance of Zirconium-based MOF-801 at varying porosity levels. The selection of Zr-MOF-801 as the focal material stems from its superior physicochemical properties, including high thermal and chemical stability, robust framework, and exceptional water adsorption capacity under low relative humidity conditions [51–53]. These characteristics make it a prime candidate for sustainable AWH, particularly in arid regions. Unlike previous works [53,54], which primarily focus on experimental synthesis or limited computational studies, this research provides a comprehensive analysis of how porosity influences the fundamental adsorption and desorption mechanisms. By tailoring the porosity, the study addresses the critical trade-off between maximizing adsorption site availability and maintaining structural integrity and adsorbent density. To ensure accuracy and reliability, this study was initiated with a model validation and result verification for pristine MOF-801 by comparing MD simulation results with experimental data from Hashjin et al. [53]. Their study demonstrated the high potential of adsorption-based AWH to meet increasing water demand, highlighting MOF-801's unique structure.

The stability of MOF-801 is crucial for its performance in atmospheric water harvesting (AWH), particularly during repeated adsorption–desorption cycles, which is also fundamental to both water treatment and pollution elimination [38,55]. A stable adsorbent ensures high efficiency, longevity, and reliability over multiple cycles, making MOF-801 an ideal candidate for such applications. MOF-801 is known for its exceptional structural stability in both water and thermal environments, which is a significant advantage in atmospheric water harvesting. The fumarate backbone, a key component of MOF-801, is a highly researched material due to its low cost and remarkable stability. In a study by Hashjin et al., the thermal stability of synthesized MOF-801 was evaluated using thermogravimetric analysis (TGA). The TGA curve revealed a 23 % weight loss below ~200 °C, attributed to the removal of

adsorbed water and guest molecules trapped within the pores of the adsorbent. Beyond 350 °C, the sharp weight loss observed up to 500 °C was linked to the decomposition of fumaric acid and the breakdown of carboxylate groups, indicating that the adsorbent maintains excellent thermal stability at high temperatures. Additionally, MOF-801 demonstrates stable adsorption performance at various temperatures. In conditions with 50 % relative humidity, MOF-801 shows optimal water adsorption at 25 °C. However, as the temperature increases to 35 °C, the maximum adsorption capacity slightly decreases by 4 %. After six hours at 35 °C, signs of instability in the water adsorption behavior are observed, suggesting that while MOF-801 remains stable, prolonged exposure to higher temperatures may reduce its efficiency. Further examination of MOF-801's stability in multiple adsorption cycles highlights its resilience. After 20 cycles, the specific surface area of MOF-801 decreased by only 13 %, from its initial value of approximately 690 m<sup>2</sup>/g–600.35 m<sup>2</sup>/g. This slight reduction can be attributed to minor structural degradation or exhaustion of the adsorbent but is considered negligible in terms of its overall performance, confirming the material's excellent stability over time [53]. Moreover, in another study by Zhan et al., MOF-801 demonstrated impressive chemical stability. It showed remarkable proton conductivity ( $1.88 \times 10^{-3}$  S cm<sup>-1</sup> at 298 K and 98 % relative humidity) and excellent resistance to hydrochloric acid, sodium hydroxide solutions, and boiling water. This highlights MOF-801's robustness under challenging environmental conditions, further solidifying its potential as a reliable material for use in atmospheric water harvesting systems [56]. Overall, these findings suggest that MOF-801 is a highly stable and reliable material, exhibiting excellent thermal, water, and chemical stability. This makes it an ideal candidate for long-term applications in atmospheric water harvesting, where material stability is critical for sustainable water extraction and environmental sustainability.

Building upon this validation, MD simulations were conducted to evaluate the impact of porosities ranging from 1 % to 10 % under conditions of 80 % relative humidity. The simulations encompassed four key phases: equilibration, moisture adsorption, water release, and a second adsorption cycle, allowing for a detailed assessment of MOF-801's performance across multiple cycles. Critical parameters such as potential energy, interaction energy, enthalpy, MSD, and RMSD were analyzed to understand the interplay between porosity and water adsorption dynamics. This computational approach not only fills a significant gap in the literature regarding the impact of porosity on MOF-801 performance but also offers a scalable pathway for designing MOFs with tailored properties for efficient and sustainable AWH applications. This work is essential for advancing the understanding of structure-performance relationships in MOFs, providing a scientific basis for future innovations in water scarcity mitigation technologies.

## 2. Simulation and method

### 2.1. Molecular dynamics

Using MD simulations, scientists can accurately track the movement of individual atoms in a virtual lab. These simulations are grounded in solving Newton's equations of motion. Initially, a simulation box is populated with a finite number of atoms or molecules. MD is commonly applied to systems with hundreds or thousands of atoms, where surface effects are more noticeable. Periodic boundary conditions are used to manage these effects [57]. A critical component of MD modeling is the potential function, which defines the nature and strength of interactions between particles. Different materials have been assigned specific potential functions over time. By utilizing a detailed model of the physics governing interatomic interactions, MD simulations can predict the motion of each atom within proteins or other molecular systems over time. Newton's equations of motion incorporate the potential function, based on particle positions, to derive the forces acting on them [58].

In current study, the interactions between atoms in the MOF-801 and

atmospheric molecules are calculated using two models: the Universal Force Field (UFF) and the DREIDING Force Field. [59,60]. The UFF and DREIDING models utilize the Lennard-Jones (LJ) potential to describe non-bonded interactions between atoms, which is expressed as follows (Eq. (1)):

$$U(r_{ij}) = 4\epsilon \left[ \left( \frac{\sigma}{r_{ij}} \right)^{12} - \left( \frac{\sigma}{r_{ij}} \right)^6 \right] r_{ij} \leq r_c \quad (1)$$

In this equation,  $\epsilon$  denotes the depth of the LJ potential well,  $\sigma$  represents the finite distance at which the interatomic potential is zero, and  $r$  signifies the distance between atoms. The cut-off radius,  $r_c$ , is fixed at 12 Å across all our simulations. The specific values of  $\epsilon$  and  $\sigma$  for different atomic types used in our MD simulations can be found in Table 1 [59,60]. By utilizing the data from Table 1, the values of  $\epsilon$  and  $\sigma$  for all interactions between the particles in the simulation box can be determined.

Furthermore, the bond strengths in interactions, including simple bonds, bond angles, and dihedral angles, are modeled using a simple harmonic oscillator approach. The harmonic components of atomic bonds and angles are estimated to characterize these bonded interactions. Currently, the bonded interactions in the atmosphere-MOF (801) system are defined using a simple oscillator [59,60].

Here,  $k_r$ ,  $r_0$ ,  $k_\theta$ , and  $\theta_0$  denote the constants for the harmonic oscillator, atomic bond length, angular oscillator, and equilibrium angle value, respectively. The  $r_0$  values for different bonds in the simulation are presented in Table 2 [59,60].

Once the atomic structures are defined by the force-field, MD simulations proceed with the integration of Newton's second law to track atomic evolution over simulation time.

In typical MD simulations, the velocity Verlet algorithm (Eqs. (2) and (3)) is commonly used to solve the motion equations [61,62]. Eq. (9) describes how the coordinates  $r(t+\Delta t)$  of atoms are updated. Eq. 10 describes how the velocities  $v(t+\Delta t)$  of atoms are updated.

$$r(t + \Delta t) = r(t) + v(t)\Delta t + \frac{1}{2}a(t)(\Delta t)^2 \quad (2)$$

$$v(t + \Delta t) = v(t) + \frac{1}{2}[a(t) + a(t + \Delta t)]\Delta t \quad (3)$$

These equations illustrate the iterative process used in MD simulations to compute the positions and velocities of atoms in successive time steps.

### 2.2. Simulation details

In this study, an atmospheric mixture containing O<sub>2</sub>, N<sub>2</sub>, and 80 % humidity, was simulated within a cubic simulation box measuring 100 Å in each dimension (X, Y, and Z), as depicted in Fig. 1(a). MOF-801 with a three-dimensional structure constructed using fumarate linkers, was modeled (Fig. 1(b, c)). Each secondary building unit (SBU) of MOF-801 comprises six Zirconium ions, each coordinated with eight oxygen ions, interconnected through 12 linkers. Periodic boundary conditions were applied in all directions. The MOF-801 structure, with dimensions of 53.5 × 53.5 × 53.5 Å, was positioned at the center of the simulation box (Fig. 1(d, e, and f)) and immobilized using a spring/self-fix method with

**Table 1**

Parameters ( $\epsilon$ ,  $\sigma$ ) of the Lennard-Jones potential function for the atmosphere-MOF-801 system.

Element	$\sigma$ (Å)	$\epsilon$ (kJ/mol)
C	4.1800	0.3050
H	3.2000	0.0100
N	3.9950	0.4150
O	3.7100	0.4150
Zr	3.1240	0.0690

**Table 2**  
The  $r_0$  values for atomic bonds in simulated system.

Bond	$r_0$ (Å)
C–C	1.530
C–H	1.090
C–O	1.420
H–O	0.980
N–N	1.394
O–O	1.310
O–Zr	2.214

a spring constant of 5 kcal/mol·Å<sup>2</sup>. This setup aimed to simulate the adsorption of H<sub>2</sub>O (moisture in the air) onto MOF-801. A Zr-MOF-801 model with a unit cell dimension of 17.83 Å, obtained from the Crystallography Open Database (COD, Entry: 4121459), was utilized in this study. To simulate experimental conditions, where Zr-MOF-801 particles averaged 46 nm in size, a 3 × 3 × 3 supercell was constructed, resulting in dimensions of approximately 53.5 Å along each axis. This size was selected to capture key pore-scale adsorption phenomena while maintaining computational efficiency. The supercell represents a sufficiently large fragment of the MOF's crystalline structure, encompassing multiple pores and adsorbate-adsorbent interactions. Periodic boundary conditions were applied to simulate the bulk behavior of an infinitely extended material, bridging the gap between the nanoscale model and the macroscale experimental system. This approach aligns with established practices in molecular simulations of porous materials, where smaller representative systems are used to derive molecular-level insights.

The structural model was based on the crystallographic data reported

by Furukawa et al. (2014) in the Journal of the American Chemical Society [63]. The reported unit cell parameters ( $a = b = c = 17.834$  Å, cubic crystal system, space group Pn-3) ensure accurate representation of the material. The consistency observed between the simulation results and experimental data validates the choice of modeling scale and methodology, highlighting the ability of the simulation to reflect real-world adsorption dynamics.

#### Step 0: Minimization phase

Prior to commencing the equilibration phase, the MD simulation setup for MOF-801 and an atmospheric mixture containing O<sub>2</sub>, N<sub>2</sub>, and 80 % humidity underwent meticulous preparation and minimization to establish a stable starting point. Step 0 involved a rigorous minimization process, utilizing the conjugate gradient (CG) method within the Large-scale Atomic/Molecular Massively Parallel Simulator (LAMMPS) simulation package [64]. This iterative approach adjusted atomic positions to minimize forces and reduce potential energy towards a local minimum. Parameters were carefully set with a tolerance of 0.001 kcal/mol·Å for both force and energy convergence criteria. A maximum of 10,000 iterations and 10,000 line minimizations per iteration ensured comprehensive convergence.

#### Step 1: Equilibration phase

The simulation commenced with an equilibration phase to establish initial thermal and mechanical stability. The Nose-Hoover thermostat was employed to maintain the system's temperature at 298.5 K and pressure at 1 bar. The equilibration was performed under the NVT ensemble (constant number of particles, volume, and temperature), with a temperature damping time of 10 fs. The simulation ran for 10 ns with a time step of 0.1 fs. During this phase, critical physical parameters such as temperature, potential energy, kinetic energy, and total energy were monitored to ensure that the system reached equilibrium.

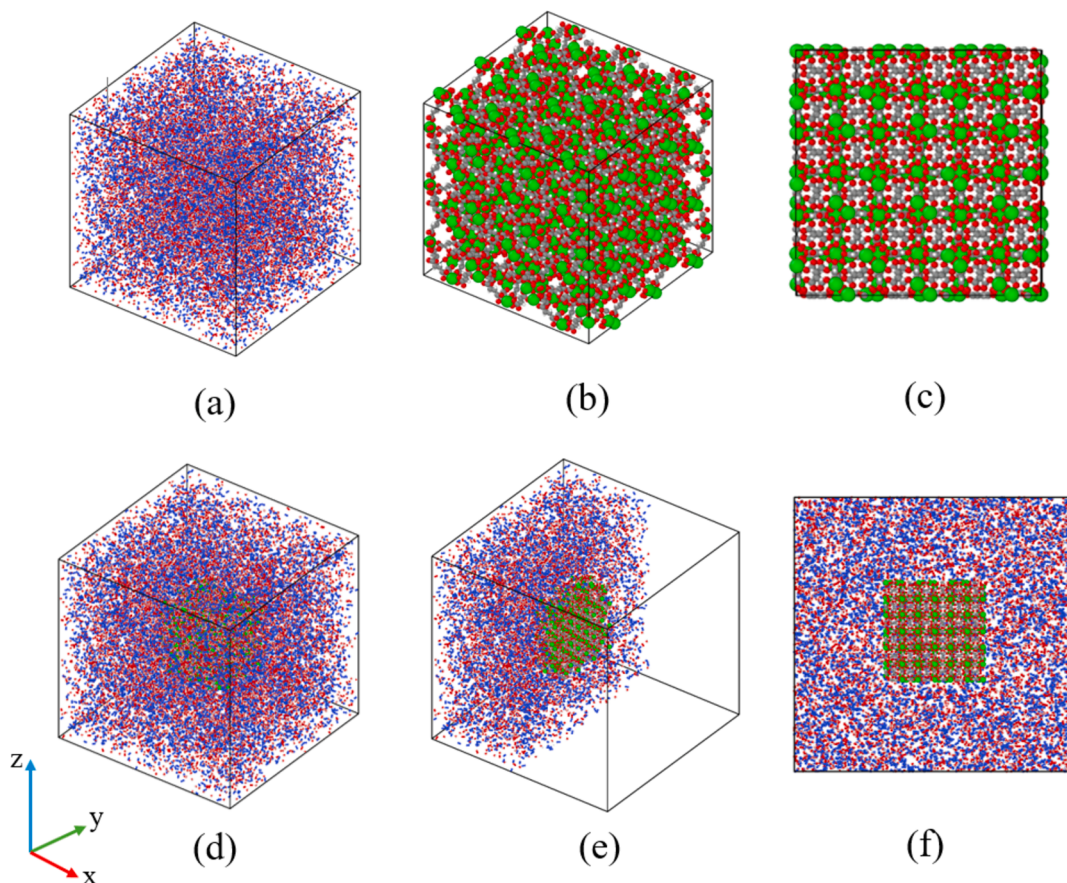


**Fig. 1.** The atomic modeling of (a) atmosphere, (b, c) MOF-801, (d) bulk system, (e, f) sliced system. The Zr, O, C, H, and N atoms are represented by the colors green, red, grey, white, and blue, respectively.

### Step 2: Adsorption phase

After achieving equilibrium conditions, the simulation was extended for an additional 10 ns to further explore the adsorption phenomena. This phase was conducted under the NVE (constant number of particles, constant volume, and constant energy) ensemble, focusing on the interactions and adsorption dynamics of H<sub>2</sub>O molecules on the MOF-801 structure. A target region was defined around the adsorbent, in the form of a 10 × 10 × 10 Å block, which was smaller than the cut-off radius of 12 Å. This region served as the focal point for adsorption during the simulation. To assess the adsorption capacity, we counted the number of water molecules (comprising hydrogen and oxygen atoms) within this region across all systems. The extended simulation allowed us to observe the temporal evolution of atomic structures, providing valuable insights into the adsorption behavior of moisture on MOF-801. This analysis enabled us to evaluate the efficiency and capacity of MOF-801 for atmospheric water harvesting (AWH). Additionally, several key parameters, including potential energy, kinetic energy, interaction energy, enthalpy, bond energy, mean squared displacement (MSD), and root mean square deviation (RMSD), were calculated to analyze the adsorption process in greater detail.

### Step 3: Water releasing phase

Following the equilibration and adsorption phases, the simulation progressed to investigate the release of water from the MOF-801 framework. This phase is pivotal for understanding the material's behavior under varying environmental conditions and its potential applications in AWH technologies. Velocity initialization was performed to ensure a consistent temperature of 298.15 K across all particles in the system, promoting uniform kinetic energy distributions essential for accurate simulations. For desorption (water release), the system temperature was raised from 298.15 K (room temperature) to 363.15 K (90 °C). The entire system was maintained under the NVT ensemble at 298.15 K, using a thermostat range of 298.15 K–363.15 K and a damping time of 100 fs to control thermal fluctuations. In this stage,

thermodynamic properties, including temperature, potential energy, kinetic energy, and total energy, were monitored and recorded. The number of water molecules (hydrogen and oxygen atoms) that are released during increasing temperature was recorded. This quantity helps understand the ability to retain adsorbed water, desorption capacity, and reusability of the MOF-801 samples.

### Step 4: 2nd Cycle of adsorption

After completing the water releasing phase, we proceeded with a second cycle of adsorption to further explore the dynamics of moisture adsorption onto MOF-801. Following the water releasing, our newly dried MOF-801 was once again fixed at the center of the simulation box using the spring/self-fix method, mirroring the initial setup. This ensured consistency in simulation conditions between cycles, facilitating a comparative analysis of adsorption behaviors under various water adsorption cycles. This approach allowed us to gain deeper insights into the temporal evolution of atomic structures and to evaluate the effectiveness and capacity of MOF-801 in AWH multiple times.

## 3. Results and Discussion

### 3.1. Pristine MOF-801

In the initial part of this study, the performance of pristine MOF-801 for AWH is investigated. Following the procedures outlined in the previous section (Section 2.2. Simulation details), the system is equilibrated after minimization, with modeled pristine MOF-801 fixed at the center of a modeled atmosphere at 80 % humidity. During the equilibration stage, several key thermodynamic properties are monitored to ensure that the system reaches a stable state. The system temperature was observed to stabilize at the target value of 298.5 K, as shown in Fig. 2(a), indicating successful thermal equilibration. Achieving a stable temperature is crucial for representing realistic environmental conditions and for ensuring that the kinetic energy distribution of the system matches

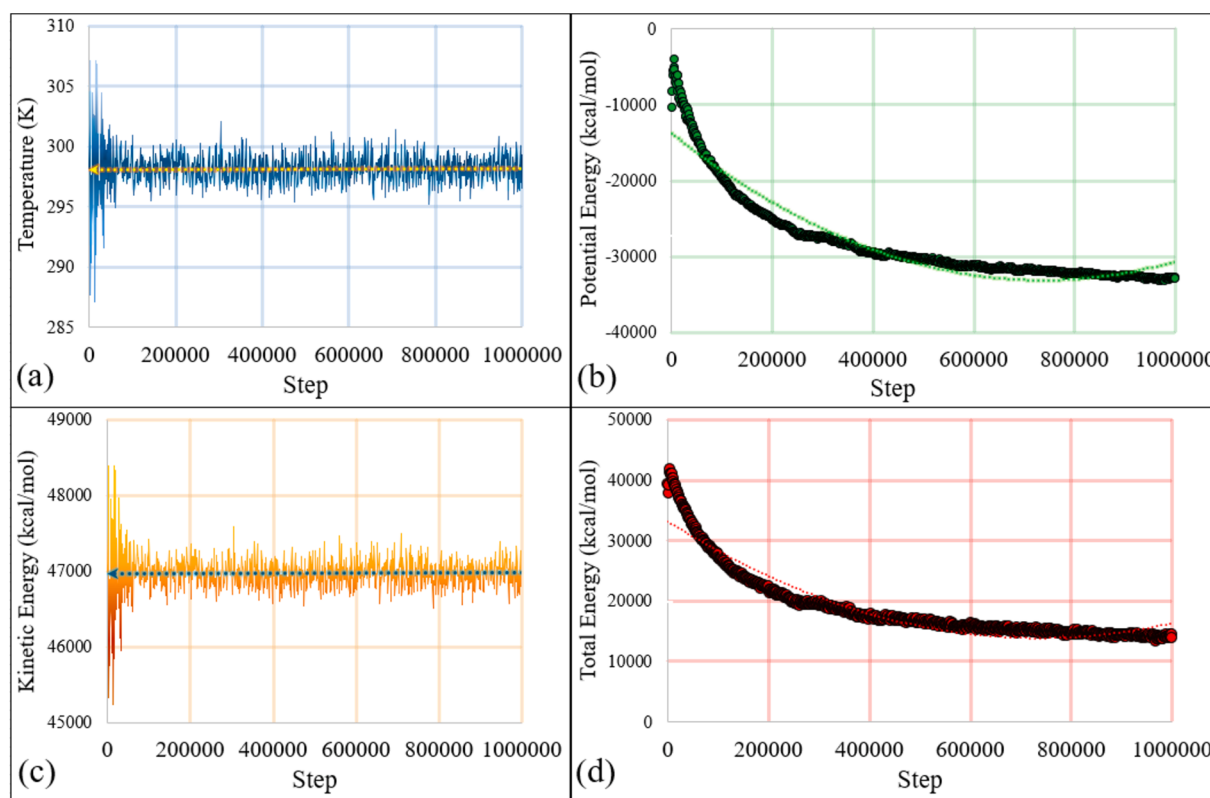


**Fig. 2.** Thermodynamical properties changes during the equilibration stage: (a) Temperature, (b) potential energy, (c) kinetic energy, and (d) total energy of the simulated system.

the desired thermodynamic state. Fig. 2(b) shows the potential energy, which started at approximately  $-3989.5$  kcal/mol and decreased to around  $-33239$  kcal/mol by the end of the equilibration phase. This significant reduction and subsequent stabilization of potential energy indicate that the system reached a stable configuration. The initial high potential energy is typically due to unfavorable interactions between molecules or atoms in the early stages of the simulation. As the system evolves and particles rearrange, potential energy decreases, reflecting the establishment of more stable, energetically favorable interactions within the system [65]. Moreover, the kinetic energy, depicted in Fig. 2(c), converged to approximately 47,000 kcal/mol at the end of equilibration, further confirming the system's stability. Kinetic energy, which is associated with the motion of particles, stabilizes as the system temperature equilibrates [66]. This stability is a sign that the system has reached a balanced state where the input of thermal energy matches the system's energy dissipation. Furthermore, the total energy of the system, as shown in Fig. 2(d), decreased from an initial value of 41761.165 kcal/mol and stabilized at around 13410.743 kcal/mol by the end of the equilibration phase. The observed trend of decreasing total energy reflects the system's progression toward a more stable, lower-energy state, characteristic of equilibration. Total energy, which is the sum of kinetic and potential energies, serves as a comprehensive measure of the system's overall energy status. Its stabilization signifies that the system has reached a steady state, with minimal fluctuations in energy. This successful equilibration ensured that both the MOF-801 structure and the surrounding atmospheric mixture achieved a stable and representative state, providing an appropriate foundation for the subsequent adsorption simulations. Stabilizing these thermodynamic properties is crucial, as it establishes a reliable starting point for the in-depth analysis of water adsorption mechanisms in the MOF-801 structure under the specified atmospheric conditions.

After reaching equilibrium in the system, the simulation of moisture adsorption from air (water molecules comprising hydrogen and oxygen) in the NVE ensemble begins. This comparison serves as model validation and proof of the simulation process. As shown in Fig. 3(a), the adsorption process accelerates rapidly at the start of the simulation, achieving equilibrium at around 0.1 simulation time. The rapid adsorption rate observed can be attributed to the numerous adsorption sites on the surface of MOF-801 and the intrinsic pores of pristine MOF-801, which facilitate the penetration of water molecules onto and within the adsorbent surface. Once the system reaches its maximum adsorption, with 4172 H<sub>2</sub>O molecules adsorbed as indicated by the simulation, the adsorption capacity starts to plateau. However, on average, the number of water molecules adsorbed by pristine MOF-801 during the simulation period is 3771. The accuracy of these simulation results is assessed by comparing them with findings from previous studies. Notably, the work of Aghajani Hashjin et al., who investigated the synthesis of MOF-801 using green synthesis and solvothermal methods for AWH, is referenced for validation [53]. This comparison suggests that the results are reasonably accurate. Additionally, the adsorption capacities are converted to ensure consistency in the comparison.

Fig. 3(b) depicts the changes in potential energy throughout the simulation's adsorption phase, starting from a maximum value of  $-7666.8203$  kcal/mol and decreasing to a minimum value of  $-13777.1$  kcal/mol by the end of the simulation. This sharp decline in potential energy reflects the reduction in latent energy within the system, signifying effective adsorption. As water molecules are adsorbed, their interactions with the MOF-801 structure reduce the system's overall potential energy, indicating stabilization and binding energy. This behavior can be observed in the visual output of the simulation for the indicated step in Fig. 3(c). Initially, the available adsorption sites and high surface area of MOF-801 allow rapid water uptake. However, once

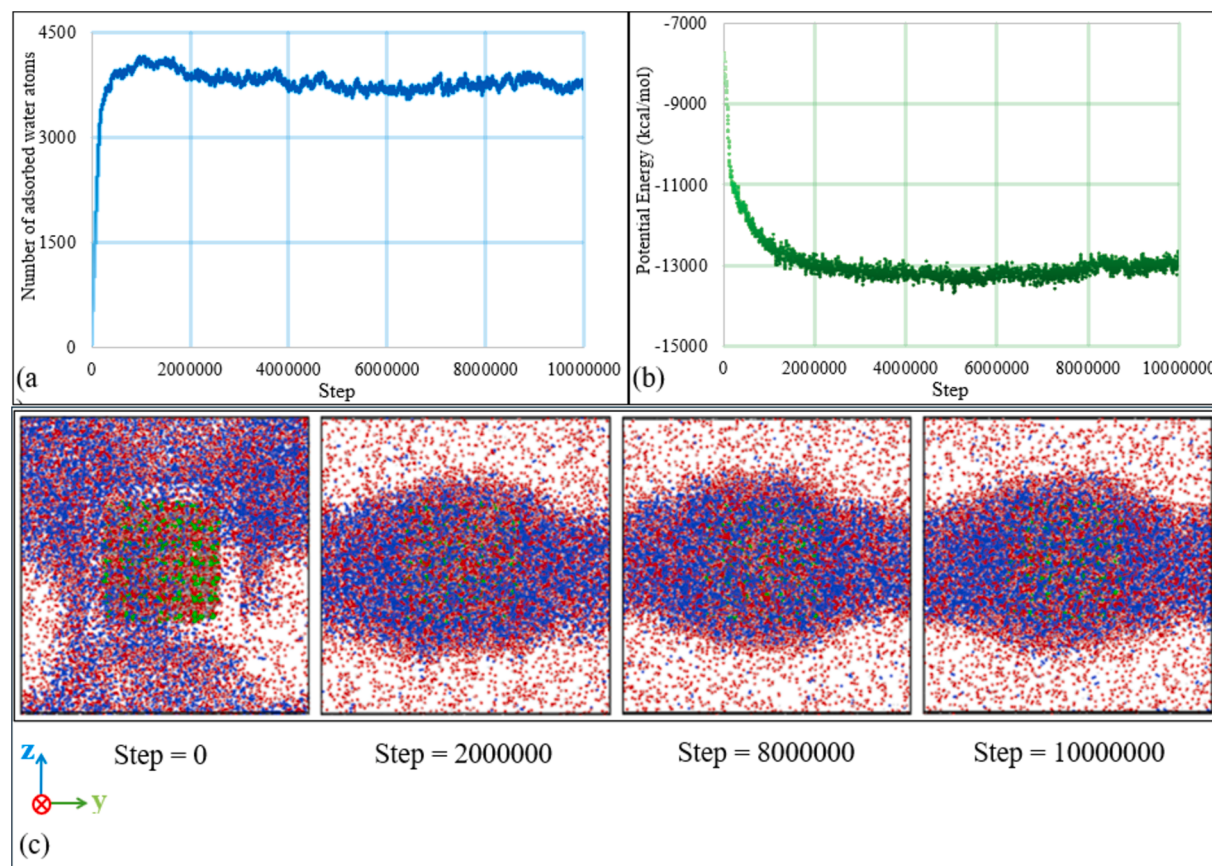


**Fig. 3.** (a) Number of adsorbed water atoms, (b) potential energy, and (c) visual outputs of the simulated system during adsorption stage. The Zr, O, C, H, and N atoms are represented by the colors green, red, grey, white, and blue, respectively.

these sites are occupied, the rate of further adsorption slows as water molecules must diffuse deeper into the structure or into less accessible pores, leading to a decrease in the overall adsorption rate. This plateau in adsorption reflects the saturation of adsorption sites [67].

The pristine MOF-801 initially adsorbs an average of 3771 water molecules from the atmosphere during the first cycle. When the temperature of MOF-801 is increased to 90 °C, the adsorbed air moisture is released as liquid water, a critical step for AWH. Both the adsorbent's capacity to take up moisture and its ability to release water upon heating are vital. Fig. 4(a) illustrates the water release process during the simulation. Initially, the adsorbed moisture is released rapidly, then the release rate increases gradually with time. The sudden release and initial spike in the desorption rate with temperature rise are due to the increased kinetic energy of water molecules, which overcomes adsorption forces, facilitating their escape from the adsorbent surface. Ultimately, as Fig. 4(a) shows, increasing the temperature to 90 °C results in an average release of 2161 H<sub>2</sub>O atoms from the initially adsorbed 3771 H<sub>2</sub>O atoms, completing the AWH process. The results demonstrate that in the first cycle, pristine MOF-801 adsorbed 47.137 % of the water molecules in the modeled atmosphere and released 57.305 % of the adsorbed moisture as water. These values are consistent with the experimental findings by Hashjin et al., thus validating the MD simulation model and process used in the present study. Moreover, Fig. 4(b) displays the potential energy during the desorption process, where the release of adsorbed moisture as water causes a sudden rise in potential energy with the release of the first H<sub>2</sub>O molecule. This rise can be attributed to the liberation of binding energy stored during adsorption, as water molecules transition from the adsorbed state back to the free

state, increasing the system's potential energy [68]. The visual output of the simulation for the specific step in Fig. 4(c) illustrates this behavior.

To gain a deeper understanding of the adsorption behavior of H<sub>2</sub>O molecules on the MOF-801 surface, it is essential to analyze both total energy and interaction energy changes throughout the simulation. Total energy provides a broad perspective on the overall stability of the system, while interaction energy specifically reveals the nature of the interactions between the adsorbate (water molecules) and the adsorbent (MOF-801). The interaction energy between water molecules and the MOF-801 framework offers a detailed view of how these molecules interact with the adsorbent during the adsorption process. This complementary analysis allows for a comprehensive understanding of the adsorption dynamics, highlighting both the macroscopic stability and the molecular-level interactions at play.

Fig. 5(a) illustrates the interaction energy between H<sub>2</sub>O molecules and the MOF-801 adsorbent throughout the adsorption simulation. At the start of the simulation, the interaction energy is relatively high (less negative), indicating that the initial interactions between H<sub>2</sub>O molecules and the MOF-801 surface are weak, as water molecules are distant or just beginning to encounter the adsorbent's surface. This stage reflects the presence of numerous available adsorption sites on MOF-801. As the simulation progresses, there is a rapid decline in the interaction energy, reaching a minimum around -1700 kcal/mol. This sharp decrease signifies the swift adsorption of water molecules onto the MOF-801 surface, where they fill the high-energy adsorption sites. The increasingly negative interaction energy suggests a stabilization process as water molecules strongly bind to the adsorbent [69]. Following this phase, the interaction energy begins to rise and fluctuates, trending towards a more

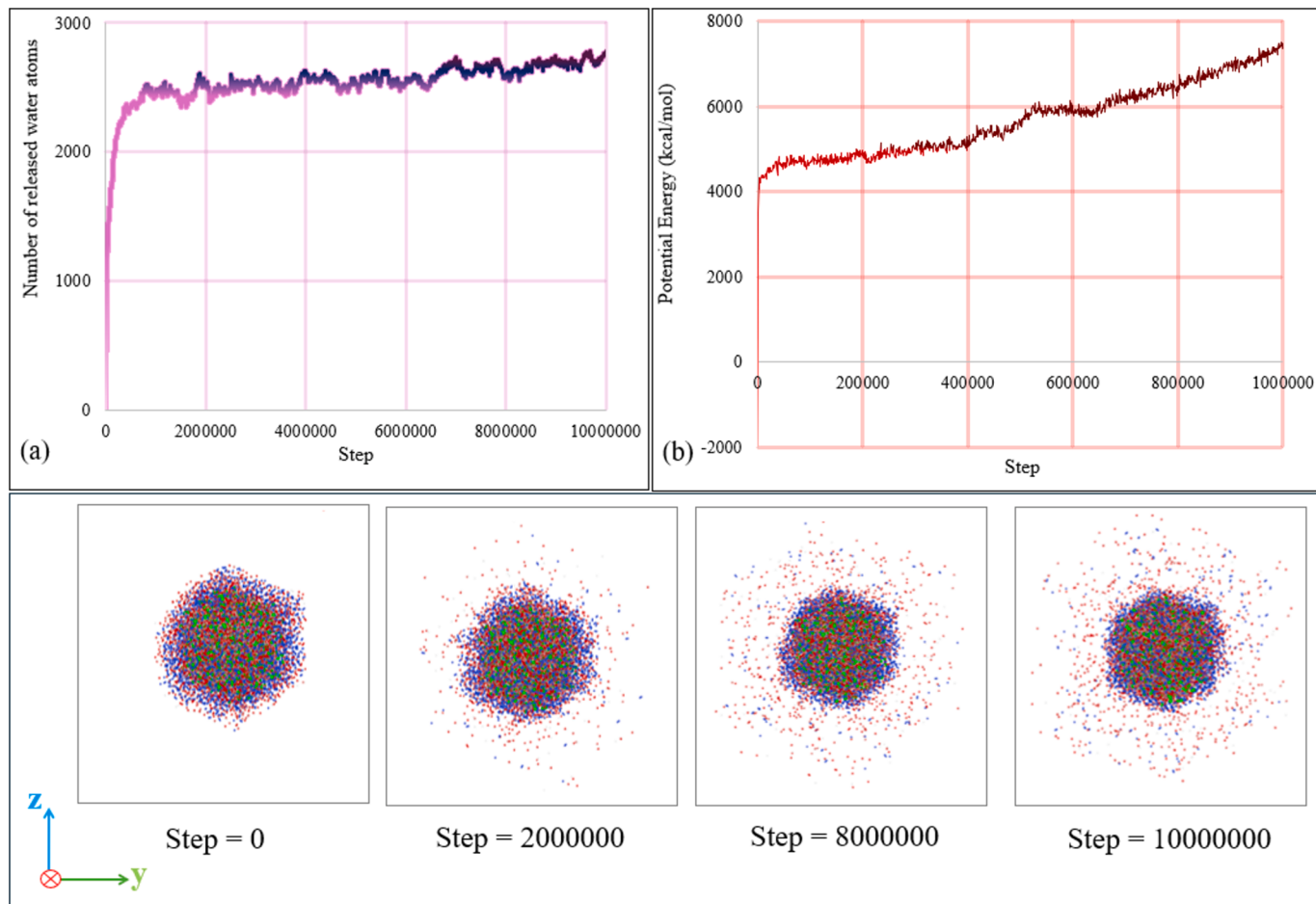


**Fig. 4.** (a) Number of released water atoms, (b) potential energy, and (c) visual outputs of the simulated system during desorption stage. The Zr, O, C, H, and N atoms are represented by the colors green, red, grey, white, and blue, respectively.

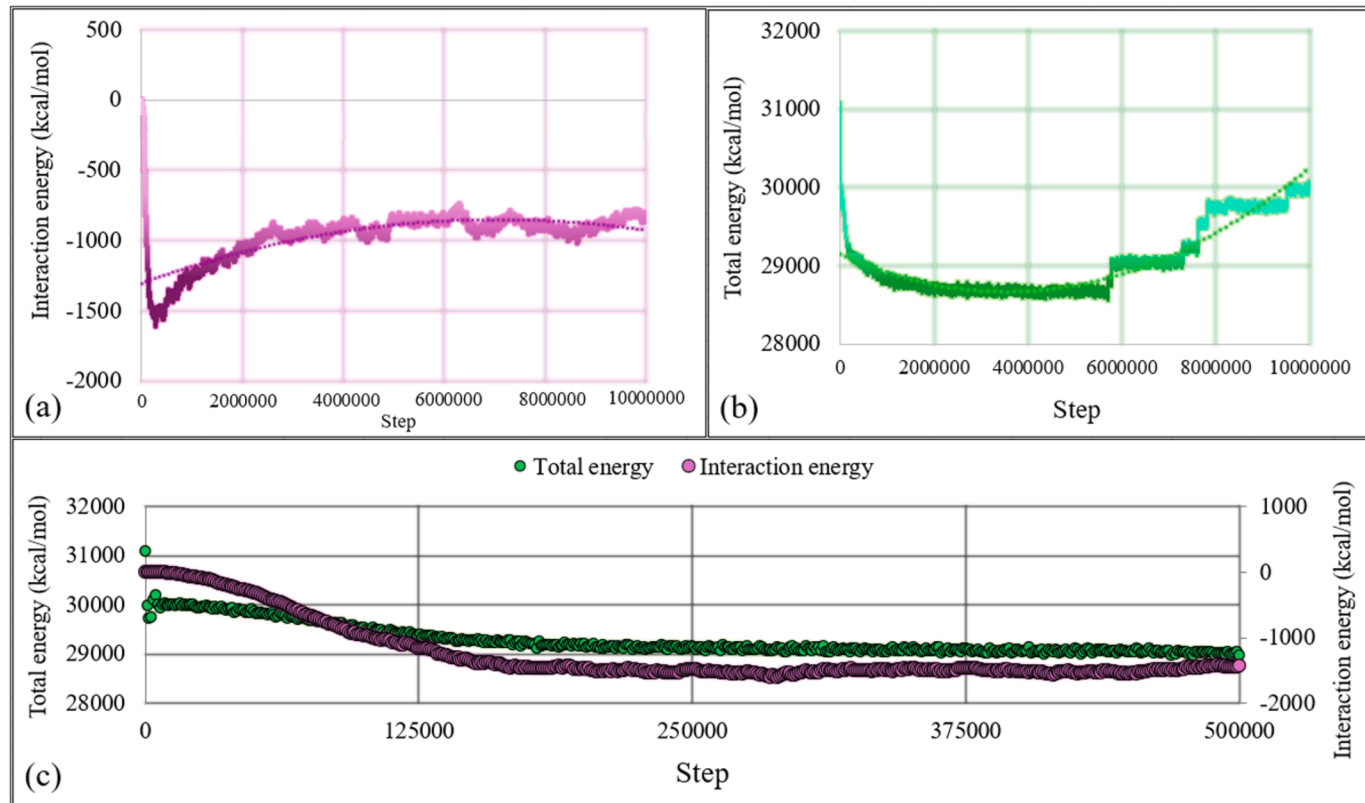


**Fig. 5.** (a) Interaction energy and (b) total energy of the simulated system during adsorption stage, and (c) during the first 5% of the simulation time.

stable and less negative range of approximately  $-1200$  kcal/mol. This pattern indicates the system is moving towards equilibrium. At this stage, most high-energy adsorption sites on the MOF-801 are occupied, and any additional adsorption involves less favorable sites or rearrangements of previously adsorbed water molecules.

In the later stages of the simulation (beyond 4,000,000 steps), the interaction energy stabilizes, oscillating between  $-1000$  and  $-1300$  kcal/mol. This stability suggests that the adsorption process has reached equilibrium, with water molecules having filled the available adsorption sites. The absence of significant changes in interaction energy indicates that the MOF-801 surface is largely saturated with  $\text{H}_2\text{O}$  molecules. The observed behavior in the plot captures the dynamics of water adsorption onto MOF-801, characterized by an initial rapid adsorption phase followed by stabilization as the system approaches equilibrium. The total energy plot during the simulation of moisture adsorption on MOF-801 is shown in Fig. 5(b) that provides critical insights into the adsorption dynamics. Initially, there is a sharp decrease in total energy, indicating the stabilization of the system as water molecules begin to adsorb onto the MOF surface. This decrease is attributed to the formation of hydrogen bonds and van der Waals interactions between water molecules and the MOF-801, leading to a lower energy state as favorable interactions develop. Following this initial stabilization, the total energy starts to increase gradually. This trend reflects the near saturation of adsorption sites on the MOF surface. As adsorption sites become occupied, additional water molecules find less favorable sites or interact with already adsorbed water layers, leading to a gradual rise in total energy. This increase suggests that further adsorption is energetically less favorable, possibly due to repulsive interactions between adsorbed molecules or structural rearrangements.

Interestingly, the energy increase follows a stepwise pattern rather than a smooth rise. These steps likely correspond to distinct adsorption events or periodic rearrangements of the adsorbed water molecules. Each step marks a specific adsorption event or reorganization, during which clusters of water molecules either form or rearrange. This leads to

temporary stability, followed by another increase in energy as the adsorption process progresses. Fig. 5(c) illustrates the changes in both total and interaction energy during the first 5 % of the simulation time, providing insights into the initial stages of water adsorption. The initial sharp decline in both total and interaction energy indicates the rapid adsorption of water molecules onto the MOF-801 surface, where strong interactions form and stabilize the system. As the high-energy adsorption sites become saturated, the energy trends level off, signaling a transition toward equilibrium. This marks a phase where the adsorption dynamics slow down, and the system stabilizes with water molecules occupying the available sites [69,70].

Ultimately, combined analysis of the total and interaction energy plots provides a comprehensive understanding of the water adsorption process on MOF-801. Based on Fig. 5(a), (b), and (c), initially, the system undergoes a rapid stabilization as water molecules fill high-energy sites, indicated by a decrease in both total and interaction energy. As the system approaches saturation, the total energy rises gradually due to less favorable interactions and structural rearrangements, while the interaction energy stabilizes, indicating equilibrium. The stepwise increase in total energy and the fluctuating interaction energy highlights the complexity of adsorption dynamics, where discrete adsorption events and molecular rearrangements play crucial roles in achieving equilibrium.

The estimated adsorption ratio for  $\text{H}_2\text{O}$  molecules in the current research using the MD method aligns well with the previous experimental findings reported by Aghajani Hashjin and colleagues [53]. In their experimental results, the adsorption ratio varies from 26.2 to 41.1 g/100 g as a function of relative humidity. Furthermore, the adsorption pattern of the target molecules is consistent with their laboratory observations [53]. This agreement between the experimental data and our computational approach validates the methodology employed in the current research, which is attributed to the appropriate configuration of various MD parameters, such as the force field, time step, temperature/pressure damping ratio, and others.

### 3.2. Effect of porosity

The influence of porosity on the efficiency of AWH using MOF-801 was investigated. Porosity is considered crucial in determining the adsorption capacity and kinetics of MOFs for water vapor under ambient conditions. The porosity of MOF-801 was systematically varied by introducing modifications of 1 %, 2 %, 3 %, 5 %, and 10 %, aiming to elucidate how changes in porosity affect the adsorption, desorption, and reusability performance. Key parameters such as the number of adsorbed water atoms, potential energy, kinetic energy, interaction energy, enthalpy, E-bond, MSD, and number of release water are analyzed to provide insights into optimizing MOF-801 for enhanced water harvesting applications. This investigation underscores the importance of porosity engineering in MOFs and advances our understanding of how material properties such as porosity can be tailored for specific technological applications through MD simulations.

#### 3.2.1. 1st cycle of adsorption

**3.2.1.1. Number of adsorbed water atoms.** In general, with the creation of porosity in the structure of the MOF-801 adsorbent, two phenomena occur, which have opposite consequences. Increasing the amount of porosity increases the empty space between atoms in the adsorbent, making it easier for the adsorbed substance to be trapped in the adsorbent. However, at the same time, the number of adsorbent atoms responsible for adsorption decreases. Essentially, when porosity increases, the number of adsorbent atom decreases. As a result, the attractive forces between the MOF-801 atoms and the water molecules in the atmosphere decrease, negatively affecting adsorption. Conversely, the amount of MOF-801 surface and the specific contact surface between the MOF-801 and the moisture increases, positively affecting the amount of adsorption [71,72]. Therefore, it is necessary to find a proper balance in the porosity by manipulating the structure and balancing these two factors that affect adsorption, or in other words, optimizing the porosity in the MOF-801 structure for AWH.

In this study, along with pristine MOF-801, five porosity rates of 1 %, 2 %, 3 %, 5 %, and 10 % were studied. As shown in Fig. 6(a), during the adsorption process in all studied systems, a sharp jump occurs at the beginning due to the presence of many active adsorption sites in MOF-801, and after that, the conditions of the adsorption process reach a state of equilibrium. On average, the number of water atoms adsorbed by pristine MOF and MOF with porosity percentages of 1 %, 2 %, 3 %, 5 %, and 10 % are 3771, 3355, 3790, 3630, 3773, and 3716, respectively. In Fig. 6(b), which corresponds to the final 0.5 % of the simulation time, these conditions can be seen more clearly. It is evident that the MOF-801 structure with 2 % porosity was able to create the best balance between factor 1 (reduction of adsorbent atoms) and factor 2 (increase of

adsorption sites). On the other hand, the system with 1 % porosity was not able to activate factor 2 which resulted in a decrease in the amount of adsorption due to factor 1.

In summary, this study demonstrates that creating porosity in MOF-801 structures influences moisture adsorption capacity in a complex manner. Next, a detailed explanation of the behavior of each system and MOF-801 structure will be provided by examining other parameters.

**3.2.1.2. Potential and kinetic energy.** Building on the analysis of water adsorption behavior in MOF-801, it is essential to further investigate the system's stability and the kinetic aspects of molecular interactions during the adsorption process. One of the most critical parameters in this analysis is the potential energy, as it provides insights into the physical stability of the system throughout the adsorption process. As the porosity in the MOF-801 structure increases, the number of available adsorption sites increases, but this also results in a greater void space between the atoms. This structural modification causes a reduction in atomic density, which in turn decreases the repulsive forces that could otherwise lead to atomic instability or structural degradation. As shown in Fig. 7(a), with an increase in porosity from 1 % to 10 %, the stability of the system during the adsorption process improves. Initially, all investigated systems, including both pristine and porous MOFs, experience a significant reduction in potential energy due to rapid and abrupt adsorption at the onset, attributed to the availability of multiple adsorption sites. However, as the porosity percentage increases, the potential energy of the system decreases overall. The average potential energy values for pristine MOFs and MOFs with porosity percentages of 1 %, 2 %, 3 %, 5 %, and 10 % are -12933.3, -17330.7, -20304.3, -20284.4, -29021.5, and -32971.8 kcal/mol, respectively. These results indicate that the system with MOF-801 at 10 % porosity exhibits significantly greater stability.

Kinetic energy in a system is directly related to the mobility of its molecules. When MOF-801 adsorbs moisture from the atmosphere, the system's mobility decreases due to the adsorption process. This phenomenon is illustrated in Fig. 7(c), which demonstrates that an increase in porosity enhances the material's capacity to adsorb and trap atmospheric moisture. Consequently, as porosity increases, the overall moisture adsorption capacity of MOF-801 decreases due to saturation effects. Although Fig. 7(c) effectively represents the kinetic energy of the entire system, the variation in the number of atoms across different systems necessitates a more accurate representation. This is provided by the full-atom kinetic energy shown in Fig. 7(d), which offers a better depiction of the system's kinetic state. The average values of kinetic energy per atom in pristine MOF and porous MOF with porosities of 1 %, 2 %, 3 %, 5 %, and 10 % are 0.7945, 0.7907, 0.7752, 0.7816, 0.7741, and 0.7730 kcal/mol, respectively.

Furthermore, Fig. 7(d) highlights the significance of porosity in the

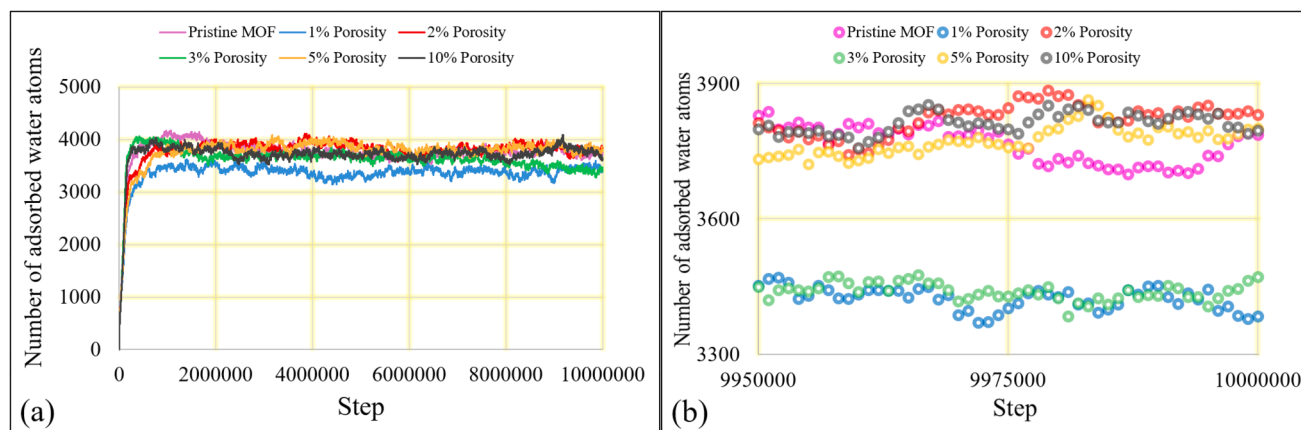


**Fig. 6.** Number of adsorbed water atoms in the simulated system (a) during the simulation time and (b) during the first 0.5% of the simulation time.

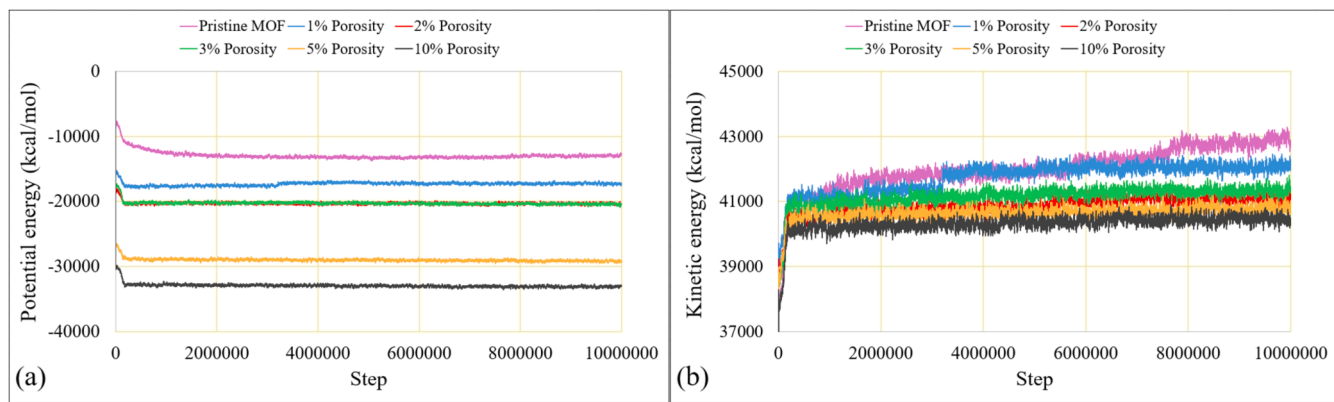


**Fig. 7.** (a) Potential energy and (b) kinetic energy of the simulated system during adsorption stage.

adsorption process, indicating that the defined pores within the MOF-801 structure actively participate in moisture uptake. The data suggest that these pores become filled with moisture rather than remaining empty, confirming that the presence of porosity facilitates the movement and subsequent adsorption of atmospheric water molecules.

**3.2.1.2.1. Interaction and bond energy.** Building on the analysis of the water adsorption behavior and system stability in MOF-801, it is crucial to investigate additional parameters that influence the adsorption process, particularly the potential and kinetic energies, which provide insights into the overall dynamics and stability of the system. One of the most critical parameters in this analysis is the potential energy, as it offers valuable information on the physical stability of the system throughout the adsorption process. As the porosity within the MOF-801 structure increases, the number of available adsorption sites increases, but this also results in greater void space between atoms, reducing the atomic density. This structural change in turn reduces repulsive forces that could otherwise lead to instability or degradation of the framework.

Another critical parameter in MD simulations is the interaction energy, which quantifies the attractive or repulsive forces between components within the system. Fig. 8(a) denotes the energy between MOF-801 and H<sub>2</sub>O molecules in the simulated atmosphere. The interaction energies averaged for pristine MOF and variants with 1 %, 2 %, 3 %, 5 %, and 10 % porosity are -964.818, -990.446, -1039.51, -953.424, -1079.38, and -965.515 kcal/mol, respectively. As previously discussed, manipulating porosity in MOF-801 involves optimizing two factors: (1) reducing the density of adsorbent atoms and (2) increasing adsorption sites. Increasing porosity and reducing adsorbent density generally decrease the interaction energy with humidity due to the predominance of factor (1). Conversely, pristine MOF, lacking porosity, shows reduced interaction energy due to the lack of factor (2) despite

potential gains in factor (1). In conclusion, our findings highlight that MOF-801 with 2 % porosity achieves an optimal balance, maximizing interaction energy with atmospheric moisture [73].

In Fig. 8(b), the bonding energy in the studied systems was investigated. Bonding energy refers to the measure of energy required to break the bonds within a material, indicating the strength and stability of those bonds. The results of the simulation and calculations show that the average bonding energies in the system with pristine MOF and MOFs with 1 %, 2 %, 3 %, 5 %, and 10 % porosity are 7390.561, 7547.393, 7451.566, 7423.313, 7404.419, and 6977.921 kcal/mol, respectively. In general, the bonding energy of the MOF-801 sample with 10 % porosity is the lowest because the number of atoms has decreased due to the definition of porosity in this absorbent sample, so the number of bonds has also decreased, leading to a decrease in bond energy. The results show that with increasing porosity, the bonding energy generally increases, except for the sample with 10 % porosity where a large number of adsorbent-adsorbent bonds are lost, significantly reducing the bond energy. MOF-801 samples with 1 % and 2 % porosity have higher bonding energies than other samples, confirming other studied parameters with the 2 % porosity sample showing better adsorption. Although the bonding energy is higher in the sample with 1 % porosity due to more bonds in the absorber itself, the sample with 2 % porosity shows that adsorbent-adsorbent bonds have changed to adsorbent-H<sub>2</sub>O bonds.

As shown in Fig. 8(b), in the pristine MOF, the bond energy starts from a lower amount compared to the MOFs with varying porosities due to several factors. Pristine MOFs maintain their original structural integrity, resulting in an initial state that is more ordered and stable, leading to lower initial bond energy because there are fewer defects and distortions within the structure. Introducing porosity into MOFs generally creates defects or vacancies within the structure, increasing the initial bond energy by disrupting the uniformity and stability of the

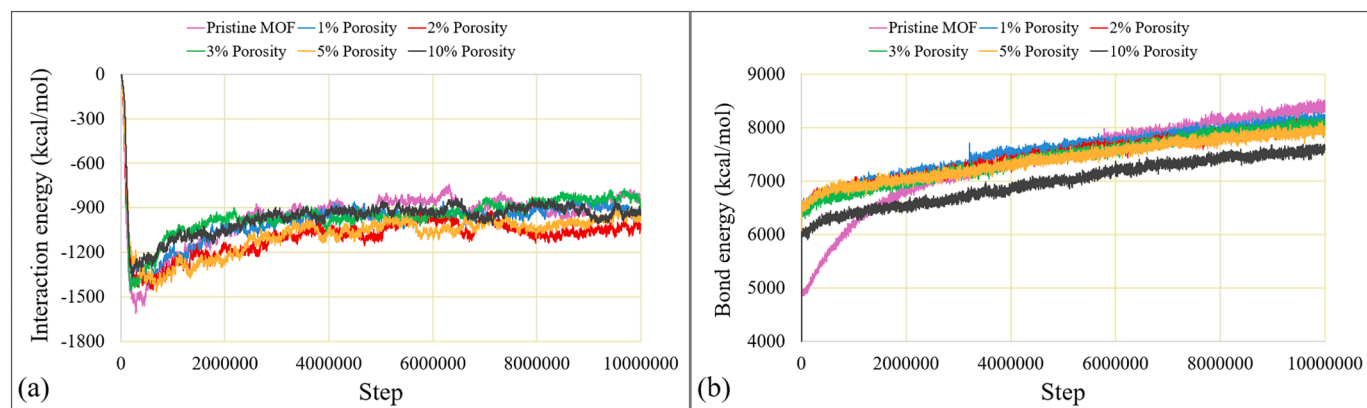


**Fig. 8.** (a) Interaction energy and (b) bond energy of the simulated system during adsorption stage.

framework, leading to higher energy states. The atomic density in pristine MOFs is higher as there are no missing links or structural voids, resulting in a lower overall bond energy initially as the energy is more uniformly distributed across a larger number of stable bonds [74].

**3.2.1.2.2. Enthalpy.** Fig. 9(a) presents the enthalpy of the system during the adsorption process, which is an important thermodynamic property that reflects the total heat content of the system. Generally, an increase in the formation of bonds, such as those between MOF-801 and water molecules, leads to an increase in the enthalpy of the system. This is because bond formation is an exothermic process, but it often results in a net increase in the enthalpy due to the energy required to break existing interactions and the overall reorganization of the system's molecular structure. As shown in Fig. 9(b), during the first 0.1 % of the simulation time, the enthalpy increases rapidly, indicating the formation of many new bonds as the adsorption sites on the MOF-801 surface become occupied by water molecules. This rapid increase is typical of the initial phase of the adsorption process, where the system is adjusting to accommodate the incoming adsorbates and establish stable interactions between the MOF structure and water. The average enthalpy values during the adsorption simulation for systems with different porosities—pristine MOFs and those with 1 %, 2 %, 3 %, 5 %, and 10 % porosity—are provided as follows: 51850.9, 50377.7, 53873, 51605.1, 44626.2, and 30331.3 kcal/mol, respectively. These values highlight the impact of porosity on the thermodynamic properties of MOF-801 during the adsorption process. Notably, the system with 2 % porosity exhibits the highest average enthalpy, indicating that the interaction between the MOF and the water molecules is stronger in this configuration.

This result suggests that introducing 2 % porosity optimizes the balance between two factors that are influenced by porosity: (1) the increase in available adsorption sites and (2) the reduction in the overall atomic density of the MOF-801 framework. With 2 % porosity, there is a greater number of adsorption sites available, which facilitates the formation of more stable bonds between the MOF and water molecules, leading to an increase in enthalpy. The stronger bond formation in this system reflects its higher stability and better adsorption strength compared to the other porosity variants.

In contrast, as the porosity increases beyond 2 %, the system's enthalpy decreases. This trend can be attributed to the fact that while more adsorption sites are created, the overall reduction in atomic density results in weaker interactions between the adsorbent and the adsorbate. Specifically, in the system with 10 % porosity, the substantial increase in void space leads to a decrease in the strength of the interaction between the MOF and water, reflected in the lower enthalpy value. Thus, the data indicate that a balance in porosity—particularly at 2 %—optimizes the adsorption strength and stability of the system, as evidenced by the higher enthalpy value. This finding supports the conclusion that moderate porosity enhances the efficiency of adsorption by facilitating stronger interactions between the adsorbent and

adsorbate, contributing to more stable and effective moisture capture by MOF-801 [75].

**3.2.1.2.3. MSD and RMSD.** MSD in atomic structures quantifies the average squared distance covered by atoms or molecules within a material over a defined period, crucial for understanding particle diffusion and mobility. By tracking individual particles' displacements from their initial positions and averaging the squared values across all particles, MSD offers insights into the material's atomic or MD [76]. In this study, MSD analyses, shown in Fig. 10 (a), predict the diffusion behavior of atmospheric moisture into the MOF-801 adsorbent. The fixed and stable structure of the adsorbent suggests that higher MSD values indicate increased penetration of water molecules into adjacent layers of the adsorbent. The MSD and RMSD values are calculated using Eqs. (4) and (5), where N represents the number of atoms,  $\vec{R}_i$  denotes the atomic positions in Angstrom units, and specifies the position of the i-th atom at time step. The MSD values for the various modeled samples are all relatively close to each other, indicating that all the samples effectively adsorb water from the atmosphere. Notably, among the various modeled samples, pristine MOF-801 exhibits the highest average MSD value of  $0.1819 \text{ \AA}^2$ .

$$MSD = \frac{1}{N} |\vec{R}_i(t) - \vec{R}_i(0)|^2 \quad (4)$$

$$RMSD = \sqrt{\frac{1}{N} |\vec{R}_i(t) - \vec{R}_i(0)|^2} \quad (5)$$

Additionally, based on Fig. 10(b), the RMSD increases to  $0.5943 \text{ \AA}$  after 10 ns. Furthermore, based on Fig. 10(c) and (d), the average MSD/RMSD ratios converge to  $0.1730 \text{ \AA}^2/0.3925 \text{ \AA}$ ,  $0.1749 \text{ \AA}^2/0.3947 \text{ \AA}$ ,  $0.1688 \text{ \AA}^2/0.3880 \text{ \AA}$ ,  $0.1663 \text{ \AA}^2/0.3847 \text{ \AA}$ , and  $0.1802 \text{ \AA}^2/0.4022 \text{ \AA}$  when porosity rates are 1 %, 2 %, 3 %, 5 %, and 10 %, respectively. These numerical results are pertinent for understanding atomic diffusion processes in practical applications. The higher MSD for pristine MOF-801 can be attributed to its unaltered and well-defined pore structure, which may allow for more straightforward diffusion pathways for water molecules. This increased mobility can lead to higher penetration of water molecules into the adsorbent layers, thus resulting in a higher MSD value. Among the modified samples, the MOF-801 with a 2 % porosity rate shows the most favorable balance in terms of water adsorption efficiency and structural stability, with an average MSD/RMSD ratio of  $0.1749 \text{ \AA}^2/0.3947 \text{ \AA}$ . This suggests that a 2 % porosity modification provides an optimal structure for effective water adsorption from the atmosphere while maintaining desirable diffusion characteristics.

In Table. 3 presents a comparison of the adsorption capacities of different materials used as adsorbents, showcasing varying performance across different studies. MOF-303 demonstrates an adsorption efficiency of 7 g/100 g [77], with another study reporting a value of 550 g/100 g

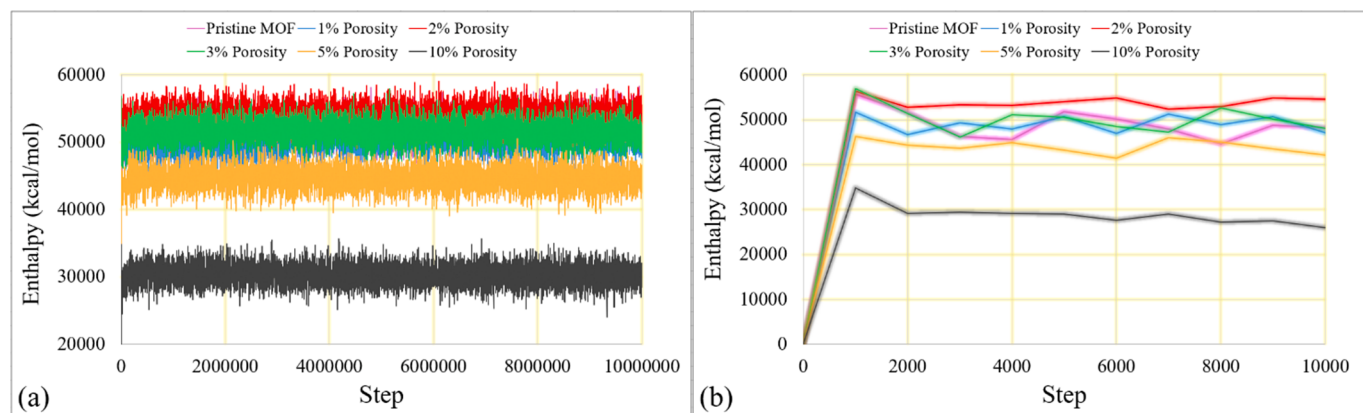


**Fig. 9.** Enthalpy in the simulated system (a) during the simulation time and (b) during the first 0.1% of the simulation time.

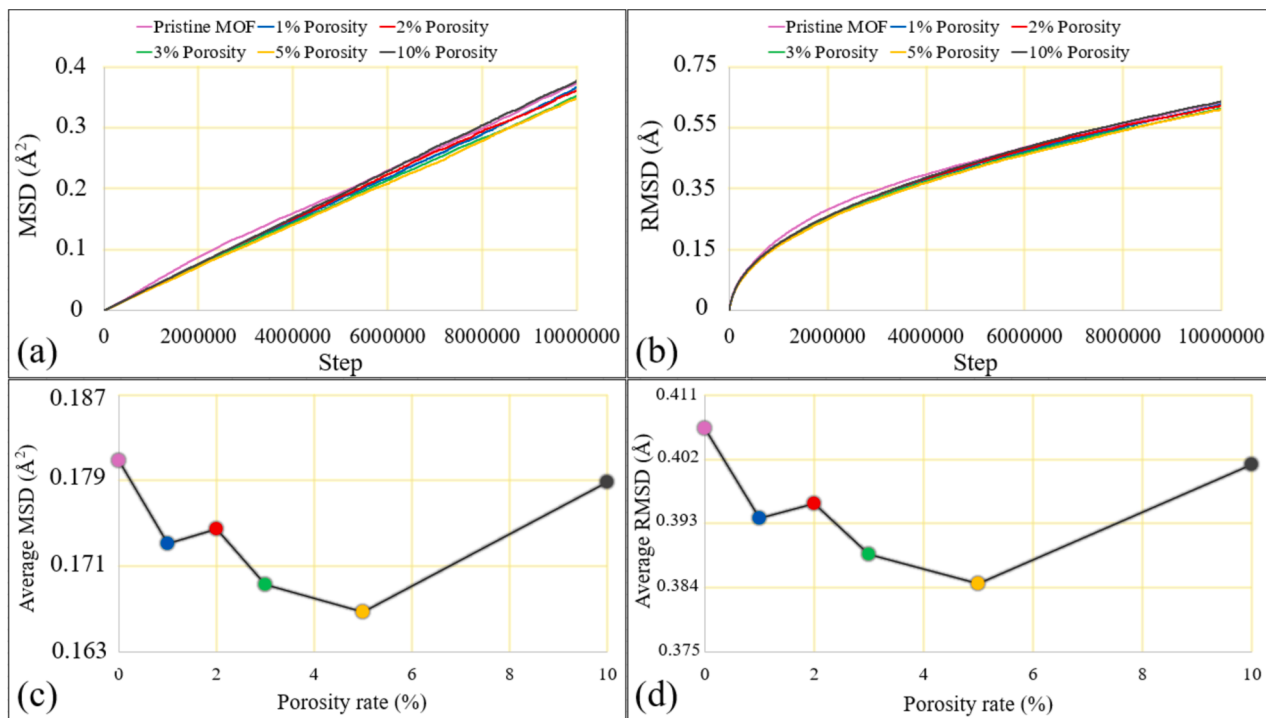


**Fig. 10.** (a) MSD and (b) RMSD of atomic system during adsorption stage, and (c) average MSD and (b) average RMSD of atomic system in different porosity rate.

**Table 3**  
Comparison of adsorption capacities of various adsorbents.

Row	Adsorbent	Converted Efficiency (g/100 g)	Reference
1	MOF-303	7	[77]
2	MOF-841	600	[78]
3	MOF-801	400	[78]
4	MOF-303	550	[78]
5	MOF-801	55.7	[79]
6	MOF-801	41.1	[53]
7	MOF-801	42.3	Current study

[78]. MOF-841 shows an adsorption capacity of 600 g/100 g [78], indicating its high efficiency. MOF-801 has several reported efficiencies: 400 g/100 g [78], 55.7 g/100 g [79], and 41.1 g/100 g [53], highlighting its versatile performance. The current study reports an adsorption efficiency of 42.3 g/100 g for MOF-801, providing a new benchmark for its performance. This comparison emphasizes the different capacities of these materials, with MOF-801 consistently showing high adsorption efficiency across multiple studies.

### 3.2.2. Desorption

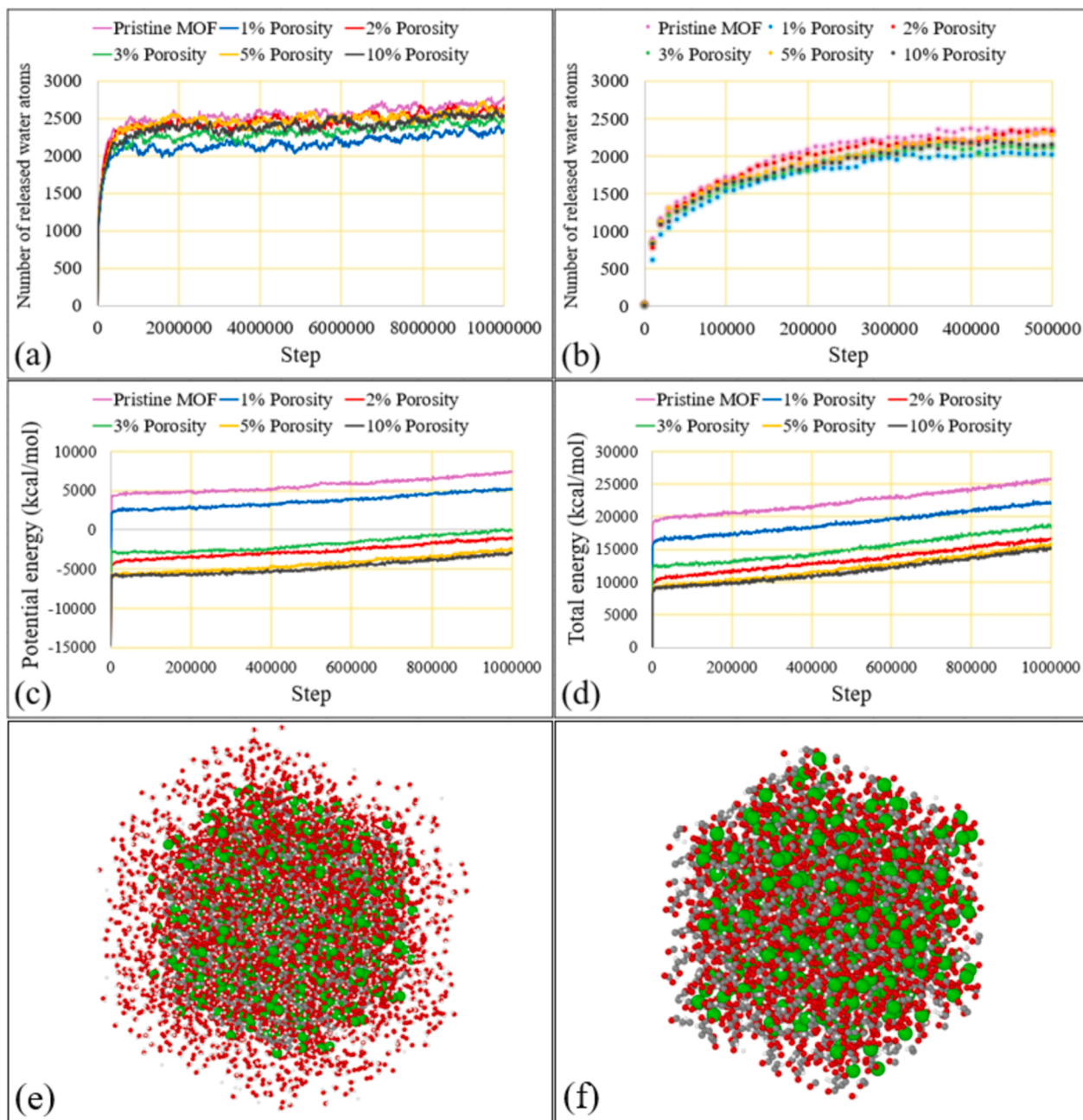
MD simulations were conducted to investigate the release behavior of water molecules from MOF-801 with varying degrees of porosity. This part of the study aimed to understand how increasing porosity affects the efficiency of water release when subjected to temperatures rising to 90 °C.

Fig. 11(a) and (b) show the number of water atoms (hydrogen and oxygen) released from the MOFs during long-term (107 steps) and short-term ( $5 \times 10^5$  steps) simulations, respectively. In both timeframes, the data reveals that MOFs with higher porosity levels release water atoms more rapidly than the pristine MOF. The average number of water atoms released throughout the simulations is 2538 for the pristine MOF, and 2161, 2452, 2301, 2443, and 2388 for MOFs with 1%, 2%, 3%, 5%, and 10% porosity, respectively. Although the pristine MOF released the highest number of water atoms due to weaker adsorption and more unstable adsorbent-water interactions, it shows a gradual increase in the

release of water molecules, stabilizing around 2500 molecules in the long-term simulation. In contrast, MOFs with higher porosity exhibit a faster initial release of water molecules, reaching peak values more quickly. This trend is consistent in both long-term and short-term simulations, where higher porosity correlates with more efficient water desorption. Notably, MOF-801 with 2 % porosity demonstrates a balanced behavior in the desorption process, showing optimal performance.

Fig. 11(c) and (d) illustrate the energy changes within the system during the desorption process, focusing on potential energy and total energy, respectively. Fig. 11(c) reveals that the pristine MOF and the MOF with 1 % porosity begin with positive potential energy. In contrast, MOFs with higher porosity levels (2 %, 3 %, 5 %, and 10 %) start with lower, often negative, potential energy. Over time, MOFs with higher porosity maintain lower potential energy levels than those with pristine or 1 % porosity, indicating that these structures are more stable and require less energy input during the desorption process. Similarly, Fig. 11(d) shows a steady increase in total energy over time. However, higher porosity MOFs exhibit a slower rate of increase in total energy, suggesting that while higher porosity slightly reduces the number of released water molecules, they require significantly less energy input than lower porosity MOFs (1 %) and pristine MOF. Fig. 11(e) and (f) offer visual representations of the adsorbent before and after the desorption process—depicting the adsorbent with adsorbed water prior to desorption and the adsorbent after water release, ready for a second cycle of adsorption.

This study demonstrates that increasing the porosity of MOFs enhances their ability to efficiently release adsorbed water molecules under elevated temperatures. MOFs with higher porosity levels (5 % and 10 %) not only release water more rapidly but also exhibit lower potential energy, indicating improved stability and reduced energy requirements for desorption. Notably, MOFs with 2 % porosity achieve an optimal balance between these factors. The MOF with 2 % porosity released more water atoms than all other porous MOFs (though slightly fewer than the pristine MOF) and required significantly less energy for desorption compared to the pristine MOF. Therefore, MOF-801 with 2 % porosity emerges as the most effective option among all the variations



**Fig. 11.** (a) Number of released water atoms during simulation time, (b) number of released water atoms during the first 5% of the simulation time, (c) changes in potential energy, and (d) changes in total energy during the simulation time. (e) the visual representation of modeled adsorbent before and (f) after the desorption process. The Zr, O, C, H, and N atoms are represented by the colors green, red, white, and blue, respectively.

tested.

### 3.2.3. 2nd cycle of adsorption

In the field of SAWH, studying adsorption processes across multiple cycles is crucial for optimizing system efficiency. While initial adsorption studies focus on reaching equilibrium and understanding the kinetics of water uptake, examining subsequent cycles provides valuable insights into the MOF's durability, regeneration capability, and long-term performance. This phase is especially important as it reflects real-world conditions, where MOFs must continuously adsorb and release water molecules effectively. Therefore, analyzing the second adsorption cycle is essential for gathering data that can inform the refinement of MOF designs and enhance the sustainability and reliability of water harvesting technologies.

As shown in Fig. 12(a), all six modeled samples demonstrate good performance in moisture absorption during the second cycle. This is attributed to two key factors: the intrinsic void space and high specific surface area of MOF-801, which enhance moisture uptake, and the efficient water release during the desorption stage. Although the effect of porosity on absorbent performance was less pronounced in the first absorption-desorption cycle, it becomes more significant in the second cycle. The models with porosity absorb notably higher quantities of water compared to the pristine model, highlighting the importance of porosity in improving MOF-801's reusability in subsequent cycles of AWH. Specifically, the number of water atoms absorbed during the second moisture absorption cycle for the pristine MOF and those with porosity percentages of 1 %, 2 %, 3 %, 5 %, and 10 % are 2968, 3465, 3674, 3626, 3477, and 3553, respectively. This demonstrates a 21.3 %

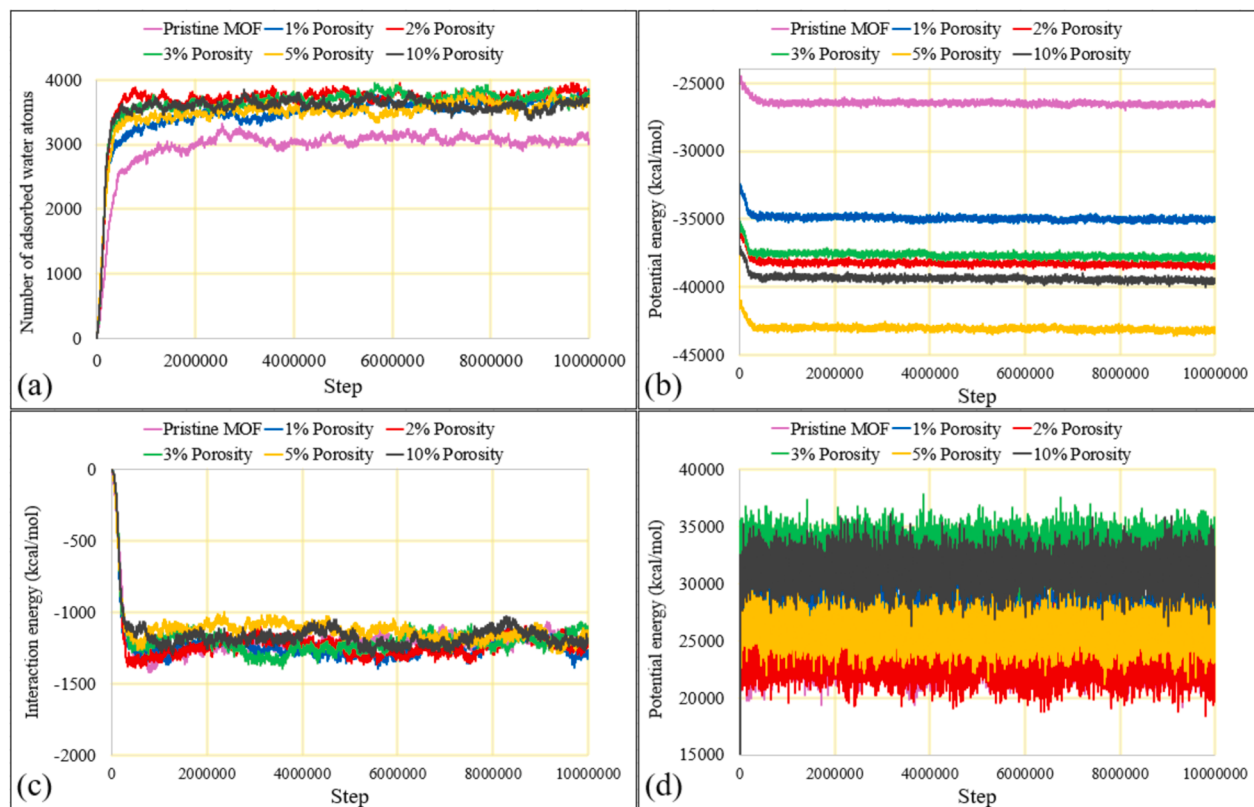


**Fig. 12.** (a) Number of adsorbed water atoms, and changes in (b) potential energy, (c) Interaction energy, and (d) enthalpy in 2nd cycle of adsorption during the simulation time.

decrease in efficiency for the pristine MOF after one cycle, while the efficiency reduction for the porous models is significantly lower: 3.27 %, 3.06 %, 0.11 %, 7.8 %, and 4.38 %, respectively. Notably, the 3 % porosity model exhibited the best performance in terms of maintaining efficiency in the second cycle, followed closely by the 2 % porosity model, which strikes a good balance among the different porosity options.

Fig. 12(b) shows the changes in the system's energy potential during the simulation, revealing much higher stability in the systems containing porosity. The significant difference in potential energy between the pristine MOF system and those with porosity suggests weaker interactions between the water molecules and the MOF structure in the pristine model, resulting in a less stable adsorption system. This is further supported by the interaction energy data shown in Fig. 12(c), which presents the energy during the second moisture absorption cycle. The average interaction energies for pristine MOF and MOF samples with 1 %, 2 %, 3 %, 5 %, and 10 % porosity are -1195.89, -1226.87, -1224.81, -1193.59, -1121.28, and -1158.31 kcal/mol, respectively. The 1 % and 2 % porosity samples show the strongest interaction between the absorbent structure and absorbed moisture, which can be attributed to a balance between removing structural atoms (which reduces available interaction sites) and increasing absorption sites and void space (which enhances absorption capacity). Among these, the 2 % porosity sample stands out as one of the best options. Conversely, the 5 % and 10 % porosity samples exhibit the lowest interaction energies, likely due to structural distortion that removes many atoms, reducing the overall interaction energy. For the pristine MOF, the limited number of adsorption sites results in fewer adsorbed water atoms and, consequently, lower interaction energy.

Fig. 12(d) illustrates the enthalpy of the system throughout the simulation, which includes both the adsorbent (MOF-801) and the adsorbed water. The 2 % porosity MOF maintains the lowest enthalpy throughout the simulation, indicating a more energetically favorable

state compared to other porosities and the pristine MOF. This lower enthalpy supports the superior performance of the 2 % porosity model in the second adsorption cycle, reinforcing its potential for enhanced AWH. In adsorption processes, enthalpy plays a crucial role as it reflects the total heat exchange; a lower enthalpy indicates a more thermodynamically efficient system. Thus, the 2 % porosity MOF stands out as the most promising material for achieving optimal performance in AWH applications.

### 3.3. Location of adsorption

To elucidate the specific adsorption sites of water molecules on the MOF-801 structure, MD simulations were conducted. The initial and final configurations of a single water molecule interacting with the MOF-801 framework are depicted in Fig. 13(a) and (b), respectively. In the initial configuration, the water molecule was positioned in close proximity to the MOF-801 framework to facilitate potential interactions. The final configuration illustrates the equilibrium state of the water molecule adsorbed on the MOF-801 framework. Detailed analysis of the simulation trajectories revealed that the hydrogen atom of the water molecule formed a stable hydrogen bond with an oxygen atom in the MOF-801 structure. This interaction is indicative of the primary adsorption site and mechanism. To further understand the adsorption mechanism, the interaction energy between the water molecule and different atoms of the MOF-801 structure was analyzed over the simulation steps. Fig. 13(c) shows the interaction energy profile between the water molecule and the oxygen, carbon, zirconium, and hydrogen atoms of the MOF-801. From the interaction energy results, the oxygen atoms of the MOF-801 exhibited the strongest interaction with the water molecules, with an average interaction energy of -0.9228 kcal/mol. This is primarily due to the ability of oxygen atoms to form strong hydrogen bonds with the hydrogen atoms of water.

Hydrogen bonds are a type of dipole–dipole interaction, where the

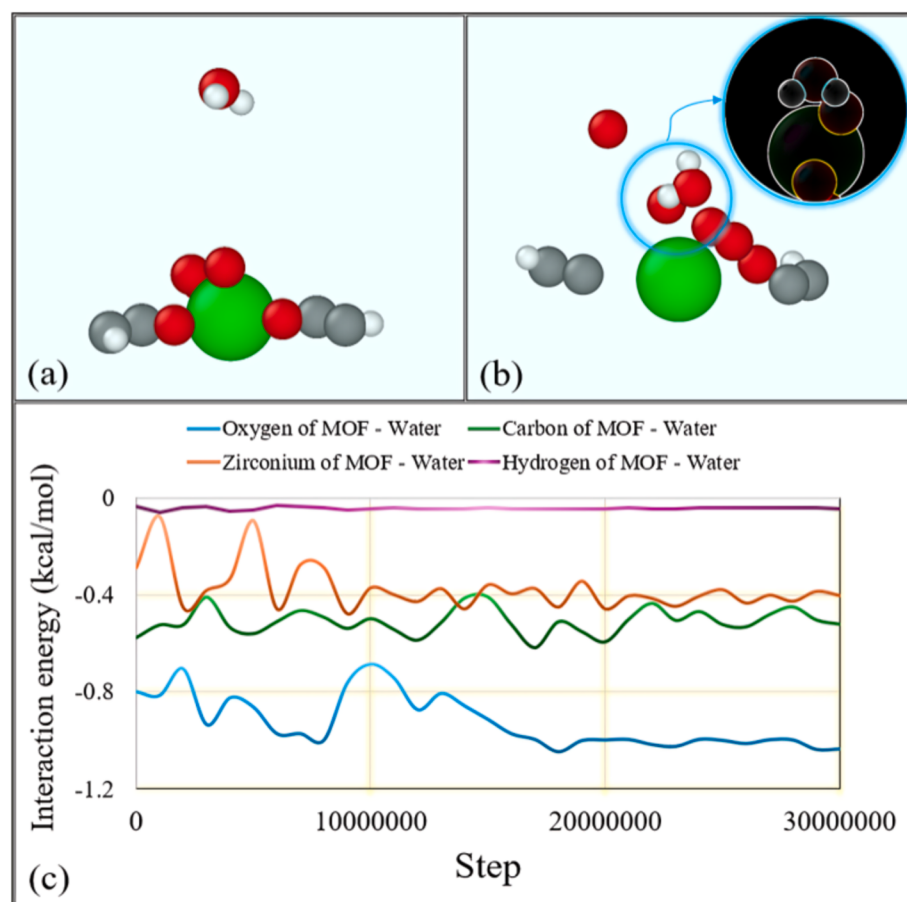


**Fig. 13.** (a) Initial configuration of a single water molecule and MOF-801 structure before the MD simulation, (b) Final configuration of the water molecule and MOF-801 structure after the MD simulation, and (c) Interaction energy between water and various atoms in the MOF-801 structure over the simulation steps.

partially positive hydrogen atoms in the water molecule are strongly attracted to the partially negative oxygen atoms in the MOF-801 framework. This strong electrostatic attraction results in a significant interaction energy, making oxygen atoms the primary adsorption sites for water molecules. The carbon atoms showed moderate interaction energies, averaging around  $-0.5085$  kcal/mol. The zirconium atoms of the MOF-801 had relatively weaker interactions with the water molecule, with an average interaction energy of  $-0.3735$  kcal/mol. The hydrogen atoms exhibited the least interaction, with values close to 0 kcal/mol, indicating minimal direct interaction. These interaction energy profiles confirm that the primary adsorption sites are the oxygen atoms of the MOF-801 framework, where strong hydrogen bonds are formed with the hydrogen atoms of the water molecule.

#### 4. Conclusion

This study provides a comprehensive analysis of how porosity engineering impacts the efficiency of MOF-801 for AWH, highlighting the critical relationship between porosity and material performance. By systematically varying the porosity of MOF-801 and analyzing key parameters, such as adsorption capacity, interaction energy, structural stability, and desorption efficiency, we show that a 2 % porosity modification optimizes the material's overall performance. MOF-801 with 2 % porosity exhibited the highest adsorption efficiency, demonstrating a favorable balance between the number of available adsorption sites and the structural integrity of the material. The interaction energy analysis confirmed that this porosity level provides the most efficient interaction between MOF-801 and water molecules, which is crucial for maximizing water adsorption from atmospheric humidity. Moreover, the potential

energy and kinetic energy analyses revealed that increasing porosity enhances the material's stability during the adsorption process. Additionally, the enthalpy and bond energy studies indicate that the 2 % porosity sample forms more stable bonds with water molecules, enhancing adsorption stability and reducing the energy required for desorption. Desorption efficiency, a key factor for practical AWH applications, was significantly improved with higher porosity, particularly at 2 %. This configuration exhibited not only rapid desorption but also lower energy requirements compared to higher porosity samples (5 % and 10 %), suggesting its suitability for energy-efficient AWH systems. Furthermore, the reusability and regeneration studies showed that MOF-801 with 2 % porosity maintains high efficiency in successive adsorption-desorption cycles, demonstrating excellent durability. The 3 % porosity sample also showed promising reusability, though slightly lower efficiency than the 2 % configuration. In conclusion, this research emphasizes the significant role of porosity in enhancing the performance of MOFs for AWH. The findings underscore that a 2 % porosity modification provides an optimal balance between adsorption efficiency, structural stability, desorption efficiency, and material reusability. This study advances our understanding of the importance of porosity engineering in tailoring MOFs for specific applications and paves the way for developing more efficient, cost-effective, and sustainable AWH systems. Future research should focus on optimizing the scalability of these materials, exploring hybrid material systems, and improving energy efficiency in both adsorption and desorption cycles. These advancements will be pivotal in addressing global water scarcity challenges and contributing to the development of sustainable technologies for AWH.

## CRediT authorship contribution statement

**Seyed Faridedin Rafie:** Writing – original draft, Visualization, Validation, Software, Methodology, Investigation, Data curation, Conceptualization. **Nidal Abu-Zahra:** Writing – review & editing, Supervision, Resources, Project administration. **Roozbeh Sabetvand:** Software, Methodology, Formal analysis, Conceptualization.

## Declaration of competing interest

The authors declare that they have no known competing financial interests or personal relationships that could have appeared to influence the work reported in this paper.

## Data availability

Data will be made available on request.

## References

- [1] H. Shemer, S. Wald, R. Semiat, Challenges and solutions for global water scarcity, *Membranes* 13 (6) (2023) 612, <https://doi.org/10.3390/membranes13060612>.
- [2] G. Wondimu Musie, G. Gonfa, Freshwater resource, scarcity, water salinity challenges, and possible remedies: a review, *Heliyon* 9 (8) (2023) e18685, <https://doi.org/10.1016/j.heliyon.2023.e18685>.
- [3] J.E.M. Baartman, G.W.J. van Lynden, M.S. Reed, C.J. Ritsema, R. Hessel, Desertification and land degradation: Origins, processes, and solutions. A literature review (DESIRE Report No. 4), ISRIC, World Soil Information, 2007.
- [4] Z. Chen, H.H. Ngo, W. Guo, S. Eslamian, Water shortages, in: *Urban Water Reuse Handbook*, first ed., CRC Press, 2015, p. 12, <https://doi.org/10.1201/b19575-13>.
- [5] E. Fernandes, R. Cunha Marques, Review of water reuse from a circular economy perspective, *Water* 15 (5) (2023) 848, <https://doi.org/10.3390/w15050848>.
- [6] C. Ingrao, R. Strippoli, G. Lagioia, D. Huisingsh, Water scarcity in agriculture: an overview of causes, impacts, and approaches for reducing the risks, *Heliyon* 9 (8) (2023) e18507, <https://doi.org/10.1016/j.heliyon.2023.e18507>.
- [7] U. Lall, L. Josset, T. Russo, A snapshot of the world's groundwater challenges, *Annu. Rev. Env. Resour.* 45 (1) (2020) 171–194, <https://doi.org/10.1146/annurev-environ-102017-025800>.
- [8] Z. Huang, X. Yuan, X. Liu, Q. Tang, Growing control of climate change on water scarcity alleviation over northern part of China, *J. Hydrol.: Reg. Stud.* 46 (2023) 101332, <https://doi.org/10.1016/j.ejrh.2023.101332>.
- [9] L.V. Noto, G. Cipolla, A. Francipane, et al., Climate change in the Mediterranean basin (Part I): induced alterations on climate forcings and hydrological processes, *Water Resour. Manag.* 37 (2023) 2287–2305, <https://doi.org/10.1007/s11269-022-03400-0>.
- [10] J. Qiu, Z. Shen, H. Xie, Drought impacts on hydrology and water quality under climate change, *Sci. Total Environ.* 858 (Part 1) (2023) 159854, <https://doi.org/10.1016/j.scitotenv.2022.159854>.
- [11] M.A.S. Azad, T. Ancev, F. Hernández-Sancho, Efficient water use for sustainable irrigation industry, *Water Resour. Manag.* 29 (2015) 1683–1696, <https://doi.org/10.1007/s11269-014-0904-8>.
- [12] A. Bhardwaj, M. Kumar, M. Alshehri, I. Keshta, A. Abugabah, S.K. Sharma, Smart water management framework for irrigation in agriculture, *Environ. Technol.* 45 (12) (2024) 2320–2334, <https://doi.org/10.1080/09593330.2022.2039783>.
- [13] S.F. Rafie, H. Sayahi, H. Abdollahi, N. Abu-Zahra, Hydrothermal synthesis of Fe3O4 nanoparticles at different pHs and its effect on discoloration of methylene blue: evaluation of alternatives by TOPSIS method, *Mater. Today Commun.* 37 (2023) 107589, <https://doi.org/10.1016/j.mtcomm.2023.107589>.
- [14] J.O. Eniola, B. Sizirci, S. Stephen, I. Yildiz, A. Khaleel, M. El Fadel, A new synthesis route of hydrothermally carbonized Na2CO3 activated bentonite clay as a novel adsorbent for cadmium removal from wastewater, *Sep. Purif. Technol.* 350 (2024) 127960, <https://doi.org/10.1016/j.seppur.2024.127960>.
- [15] Y. Duan, P. Han, R. Zhang, P. Ren, W. Shi, N.H. Wong, J. Sunarso, S. Liu, J. Yu, A CuO-modified ultrafiltration ceramic membrane inducing micro-nano bubble collapse to generate hydroxyl radicals for enhancing pollutant removal, *Appl. Surf. Sci.* 651 (2024) 159271, <https://doi.org/10.1016/j.apsusc.2023.159271>.
- [16] P. Thamarai, R. Kamalesh, A. Saravanan, P. Swaminathan, V.C. Deivayani, Emerging trends and promising prospects in nanotechnology for improved remediation of wastewater contaminants: present and future outlooks, *Environ. Nanotechnol. Monitor. Manage.* 21 (2024) 100913, <https://doi.org/10.1016/j.enmm.2024.100913>.
- [17] A.A. Adesibikan, S.S. Emmanuel, C.O. Olawoyin, P. Ndungu, Cellulosic metallic nanocomposites for photocatalytic degradation of persistent dye pollutants in aquatic bodies: a pragmatic review, *J. Organomet. Chem.* 1010 (2024) 123087, <https://doi.org/10.1016/j.jorgchem.2024.123087>.
- [18] A.R. Bhapkar, S. Bhame, A review on ZnO and its modifications for photocatalytic degradation of prominent textile effluents: synthesis, mechanisms, and future directions, *J. Environ. Chem. Eng.* 12 (3) (2024) 112553, <https://doi.org/10.1016/j.jece.2024.112553>.
- [19] S. Ajith, F. Almomani, H. Qiblawey, Emerging 2D MXene-based polymeric membranes for water treatment and desalination, *J. Environ. Chem. Eng.* 12 (2) (2024) 112078, <https://doi.org/10.1016/j.jece.2024.112078>.
- [20] X. Zhou, H. Lu, F. Zhao, G. Yu, Atmospheric water harvesting: a review of material and structural designs, *ACS Mater. Lett.* 2 (7) (2020) 671–684, <https://doi.org/10.1021/acsmaterialslett.0c00130>.
- [21] F. Zhao, X. Zhou, Y. Liu, Y. Shi, Y. Dai, G. Yu, Super moisture-absorbent gels for all-weather atmospheric water harvesting, *Adv. Mater.* 31 (10) (2019) 1806446, <https://doi.org/10.1002/adma.201806446>.
- [22] G. Raveesh, R. Goyal, S.K. Tyagi, Advances in atmospheric water generation technologies, *Energ. Convers. Manage.* 239 (2021) 114226, <https://doi.org/10.1016/j.enconman.2021.114226>.
- [23] B. Wang, X. Zhou, Z. Guo, W. Liu, Recent advances in atmospheric water harvesting: design principle, materials, devices, and applications, *Nano Today* 40 (2021) 101283, <https://doi.org/10.1016/j.nantod.2021.101283>.
- [24] T.Z. Wasti, M. Sultan, M. Aleem, et al., An overview of solid and liquid materials for adsorption-based atmospheric water harvesting, *Adv. Mech. Eng.* 14 (3) (2022), <https://doi.org/10.1177/16878132211082768>.
- [25] H. Kim, S. Yang, S.R. Rao, S. Narayanan, E.A. Kapustin, H. Furukawa, A.S. Umans, O.M. Yaghi, E.N. Wang, Water harvesting from air with metal-organic frameworks powered by natural sunlight, *Science* 356 (6336) (2017) 430–434, <https://doi.org/10.1126/science.aaf5032>.
- [26] K. Yang, T. Pan, Q. Lei, X. Dong, Q. Cheng, Y. Han, A roadmap to sorption-based atmospheric water harvesting: From molecular sorption mechanism to sorbent design and system optimization, *Environ. Sci. Tech.* 55 (10) (2021) 6542–6560, <https://doi.org/10.1021/acs.est.1c00257>.
- [27] P. Pourhakkak, M. Taghizadeh, A. Taghizadeh, M. Ghaedi, Adsorbent, in: M. Ghaedi (Ed.), *Interface Science and Technology*, vol. 33, Elsevier, 2021, pp. 71–210, doi: 10.1016/B978-0-12-818805-7.00009-6.
- [28] S.F. Rafie, H. Abdollahi, H. Sayahi, F. Doulati Ardejani, K. Aghapoor, M.H. Karimi Darvanojoghi, S.K. Brar, S. Magdouli, Genetic algorithm-assisted artificial neural network modelling for remediation and recovery of Pb (II) and Cr(VI) by manganese and cobalt spinel ferrite super nanoadsorbent, *Chemosphere* 321 (2023) 138162, <https://doi.org/10.1016/j.chemosphere.2023.138162>.
- [29] A. Mehdikhani, E. Salahi, J. Shahmoradi, Carbon/zeolite 13X composition for atmospheric water harvesting (AWH) application in arid regions, *Adsorption* (2024), <https://doi.org/10.1007/s10450-024-00476-5>.
- [30] A.K. Sleiti, H. Al-Khwaja, H. Al-Khwaja, M. Al-Ali, Harvesting water from air using adsorption material – prototype and experimental results, *Sep. Purif. Technol.* 257 (2021) 117921, <https://doi.org/10.1016/j.seppur.2020.117921>.
- [31] T. Lyu, Z. Wang, R. Liu, K. Chen, H. Liu, Y. Tian, Macroporous hydrogel for high-performance atmospheric water harvesting, *ACS Appl. Mater. Interfaces* 14 (28) (2022) 32433–32443, <https://doi.org/10.1021/acsami.2c04228>.
- [32] A.M. Alsuhaihani, A.A. Alayyafi, L.A. Albedair, M.G. El-Desouky, A.A. El-Bindary, Efficient fabrication of a composite sponge for Cr(VI) removal via citric acid cross-linking of metal-organic framework and chitosan: adsorption isotherm, kinetic studies, and optimization using Box-Behnken design, *Mater. Today Sust.* 26 (2024) 100732, <https://doi.org/10.1016/j.mtsust.2024.100732>.
- [33] F. Trapani, A. Polyzoidis, S. Loebbecke, C.G. Piscopo, On the general water harvesting capability of metal-organic frameworks under well-defined climatic conditions, *Micropor. Mesopor. Mater.* 230 (2016) 20–24, <https://doi.org/10.1016/j.micromeso.2016.04.040>.
- [34] Y. Geng, S. Hao, X. Liu, Z. Jia, S. Zheng, Water harvesting from air by MOF-801/PES porous composite membranes, *Desalin. Water Treat.* 160 (2019) 57–64, <https://doi.org/10.5004/dwt.2019.24356>.
- [35] W. Xu, O.M. Yaghi, Metal-organic frameworks for water harvesting from air, anywhere, anytime, *ACS Cent. Sci.* 6 (8) (2020) 1348–1354, <https://doi.org/10.1021/acscentsci.0c00678>.
- [36] Y. Hu, Y. Wang, Z. Fang, X. Wan, M. Dong, Z. Ye, X. Peng, MOF supraparticles for atmospheric water harvesting at low humidity, *J. Mater. Chem. A* 10 (34) (2022) 15116–15126, <https://doi.org/10.1039/D2TA02026B>.
- [37] O.M. Aldhuaiash, M.R. Shaik, S.F. Adil, Photo-induced preparation of Ag@MOF-801 composite based heterogeneous nanocatalyst for the production of biodiesel, *Catalysts* 12 (5) (2022) 533, <https://doi.org/10.3390/catal12050533>.
- [38] H.M. Nassef, G.A.A.M. Al-Hazmi, A.A. Alayyafi, M.G. El-Desouky, A.A. El-Bindary, Synthesis and characterization of new composite sponge combining metal-organic framework and chitosan for the elimination of Pb(II), Cu(II), and Cd(II) ions from aqueous solutions: Batch adsorption and optimization using Box-Behnken design, *J. Mol. Liq.* 394 (2024) 123741, <https://doi.org/10.1016/j.molliq.2023.123741>.
- [39] I. Salahshoori, S. Mahdavi, Z. Moradi, M. Otadi, F. Zare Kazemabadi, M.A.L. Nobre, H.A. Khonakdar, A. Baghban, Q. Wang, A.H. Mohammadi, Advancements in molecular simulation for understanding pharmaceutical pollutants adsorption: a state-of-the-art review, *J. Mol. Liq.* 410 (2024) 125513, <https://doi.org/10.1016/j.molliq.2024.125513>.
- [40] I. Salahshoori, Q. Wang, M.A.L. Nobre, A.H. Mohammadi, E.A. Dawi, H. Khonakdar, Molecular simulation-based insights into dye pollutant adsorption: a perspective review, *Adv. Colloid Interface Sci.* 333 (2024) 103281, <https://doi.org/10.1016/j.cis.2024.103281>.
- [41] H. Hayashi, S. Maeda, T. Mita, Quantum chemical calculations for reaction prediction in the development of synthetic methodologies, *Chem. Sci.* 14 (2023) 11601–11616, <https://doi.org/10.1039/D3SC03319H>.
- [42] L. Dong, Z. Gao, N. Lin, Self-assembly of metal-organic coordination structures on surfaces, *Prog. Surf. Sci.* 91 (3) (2016) 101–135, <https://doi.org/10.1016/j.progsurf.2016.05.001>.
- [43] N.E. Hira, S.S.M. Lock, N.F. Shoparwe, I.S.M. Lock, L.G. Lim, C.L. Yiin, Y.H. Chan, M. Hassam, Review of adsorption studies for contaminant removal from

- wastewater using molecular simulation, *Sustainability* 15 (2) (2023) 1510, <https://doi.org/10.3390/su15021510>.
- [44] M. Farajpour Mojdehi, S.F. Rafie, N. Abu-Zahra, O. Saghatelian, Z. Shams Ghamsari, F. Mahmoudi, H. Sayahi, S.M. Hashemianzadeh, Exploring the mechanisms of diazinon adsorption onto alpha and beta cyclodextrins through molecular dynamics simulations: Insights into environmentally friendly pesticide remediation, *Results Eng.* 21 (2024) 102020, <https://doi.org/10.1016/j.rineng.2024.102020>.
- [45] R. Pelalak, R. Soltani, Z. Heidari, H. Alinezhad, Synthesis, molecular dynamics simulation and adsorption study of different pollutants on functionalized mesosilica, *Sci. Rep.* 11 (2021) 1967, <https://doi.org/10.1038/s41598-020-80566-w>.
- [46] M. Dadashi Firouzjaei, F. Akbari Afkhami, M. Rabbani Esfahani, C.H. Turner, S. Nejati, Experimental and molecular dynamics study on dye removal from water by a graphene oxide-copper-metal organic framework nanocomposite, *J. Water Process Eng.* 34 (2020) 101180, <https://doi.org/10.1016/j.jwpe.2020.101180>.
- [47] S.F. Rafie, N. Abu-Zahra, R. Sabetvand, Enhancing Zn (II) recovery efficiency: Bivalent nickel–cobalt ferrite spinel Ni<sub>x</sub>Co<sub>1-x</sub>Fe<sub>2</sub>O<sub>4</sub> as a game-changing adsorbent—an experimental and computational study, *Chemosphere* 362 (2024) 142702, <https://doi.org/10.1016/j.chemosphere.2024.142702>.
- [48] J.A.R. Willenssen, S.C.B. Myneni, J.C. Bourg, Molecular dynamics simulations of the adsorption of phthalate esters on smectite clay surfaces, *J. Phys. Chem. C* 123 (22) (2019) 13624–13636, <https://doi.org/10.1021/acs.jpcc.9b01864>.
- [49] Y. Li, J. Yu, Y. Li, J. Shen, M. Du, X. Zhang, H. Zhao, J.H. Pu, Nanoporous MOF-303 performance for atmospheric water harvesting in the presence of airborne contaminants: GCMC and DFT simulations, *ACS Appl. Nano Mater.* 7 (20) (2024). <https://pubs.acs.org/doi/full/10.1021/acsnano.4c04357>.
- [50] S.K. Sibie, M.F. El-Amin, S. Sun, Modeling of water generation from air using anhydrous salts, *Energy* 14 (13) (2021) 3822, <https://doi.org/10.3390/en14133822>.
- [51] D.M. Venturi, M.S. Notari, R. Bondi, E. Mosconi, W. Kaiser, G. Mercuri, G. Giambastiani, A. Rossin, M. Taddei, F. Costantino, Increased CO<sub>2</sub> 22 affinity and adsorption selectivity in MOF-801 fluorinated analogues, *ACS Appl. Mater. Interfaces* 14 (36) (2022), <https://doi.org/10.1021/acsami.2c11562>.
- [52] M. Saidi, P.H. Ho, P. Yadav, F. Salles, C. Charnay, L. Girard, L. Boukli-Hacene, P. Trems, Zirconium-Based Metal Organic Frameworks for the Capture of Carbon Dioxide and Ethanol Vapour. A comparative study, *Molecules* 26 (24) (2021) 7620, <https://doi.org/10.3390/molecules26247620>.
- [53] M. Aghajani Hashjin, S. Zarshad, H.B. Motejadded Emrooz, et al., Enhanced atmospheric water harvesting efficiency through green-synthesized MOF-801: a comparative study with solvothermal synthesis, *Sci. Rep.* 13 (2023) 16983, <https://doi.org/10.1038/s41598-023-44367-1>.
- [54] N. Naleem, S. Kirmizialtin, N. Alkhathib, Molecular simulations on atmospheric water harvesting using adsorbents, Paper presented at the Seventh International Conference on Multifunctional, Hybrid & Nanomaterials (HYMA 2022), 2022. SSRN. doi: [10.2139/ssrn.4253342](https://doi.org/10.2139/ssrn.4253342).
- [55] S.F. Rafie, N. Abu-Zahra, M. Sillanpää, A comprehensive review of spinel ferrites and their magnetic composites as highly efficient adsorbents of rare earth elements, *Emerging Contam.* 11 (1) (2025) 100429, <https://doi.org/10.1016/j.emcon.2024.100429>.
- [56] J. Zhang, H.-J. Bai, Q. Ren, H.-B. Luo, X.-M. Ren, Z.-F. Tian, S. Lu, Extra water- and acid-stable MOF-801 with high proton conductivity and its composite membrane for proton-exchange membrane, *ACS Appl. Mater. Interfaces* 10 (34) (2018), <https://doi.org/10.1021/acsami.8b11763>.
- [57] S.A. Hollingsworth, R.O. Dror, Molecular dynamics simulation for all, *Neuron* 99 (6) (2018) 1129–1143, <https://doi.org/10.1016/j.neuron.2018.08.011>.
- [58] S.A. Adcock, J.A. McCammon, Molecular dynamics: Survey of methods for simulating the activity of proteins, *Chem. Rev.* 106 (5) (2006) 1589–1615, <https://doi.org/10.1021/cr040426m>.
- [59] S.L. Mayo, B.D. Olafson, W.A. Goddard, DREIDING: A generic force field for molecular simulations, *J. Phys. Chem.* 94 (16) (1990) 8897–8909, <https://doi.org/10.1021/j100389a010>.
- [60] A.K. Rappe, C.J. Casewit, K.S. Colwell, W.A. Goddard III, W.M. Skiff, UFF, a full periodic table force field for molecular mechanics and molecular dynamics simulations, *J. Am. Chem. Soc.* 114 (25) (1992) 10024–10035, <https://doi.org/10.1021/ja00051a040>.
- [61] R. Bozorgpour, S. Sheybani Kashani, M. Mohebi, Exploring the role of molecular dynamics simulations in most recent cancer research: Insights into treatment strategies, 2023. arXiv. doi: 10.48550/arXiv.2310.19950.
- [62] L. Verlet, Computer “experiments” on classical fluids. I. Thermodynamical properties of Lennard-Jones molecules, *Phys. Rev.* 159 (1) (1967) 98–103, <https://doi.org/10.1103/PhysRev.159.98>.
- [63] H. Furukawa, F. Gándara, Y.-B. Zhang, J. Jiang, W.L. Queen, M.R. Hudson, O. M. Yaghi, Water adsorption in porous metal–organic frameworks and related materials, *J. Am. Chem. Soc.* 136 (11) (2014) 4369–4381, <https://doi.org/10.1021/ja500330a>.
- [64] A.P. Thompson, H.M. Aktulgä, R. Berger, D.S. Bolintineanu, W.M. Brown, P. S. Crozier, P.J. in ’t Veld, A. Kohlmeier, S.G. Moore, T.D. Nguyen, R. Shan, M. J. Stevens, J. Tranchida, C. Trott, S.J. Plimpton, LAMMPS – a flexible simulation tool for particle-based materials modeling at the atomic, meso, and continuum scales, *Comput. Phys. Commun.* 271 (2022) 10817, <https://doi.org/10.1016/j.cpc.2021.10817>.
- [65] H. Akkbarzade, G.A. Parsafar, Y. Bayat, Structural stability of nano-sized crystals of HMX: a molecular dynamics simulation study, *Appl. Surf. Sci.* 258 (7) (2012) 2226–2230, <https://doi.org/10.1016/j.apsusc.2011.08.101>.
- [66] E. Ustinov, Kinetic Monte Carlo approach for molecular modeling of adsorption, *Curr. Opin. Chem. Eng.* 24 (2019) 1–11, <https://doi.org/10.1016/j.coche.2018.12.004>.
- [67] M.S. Khosrowshahi, M.A. Abdol, H. Mashhadimoslem, The role of surface chemistry on CO<sub>2</sub> adsorption in biomass-derived porous carbons by experimental results and molecular dynamics simulations, *Sci. Rep.* 12 (2022) 8917, <https://doi.org/10.1038/s41598-022-12596-5>.
- [68] L.T. Roling, F. Abild-Pedersen, Structure-sensitive scaling relations: Adsorption energies from surface site stability, *ChemCatChem* 10 (8) (2018) 1643–1650, <https://doi.org/10.1002/cctc.201800092>.
- [69] A.S. Raman, A. Vojvodic, Energy trends in adsorption at surfaces, in: W. Andreoni, S. Yip (Eds.), *Handbook of Materials Modeling*, Springer, 2020, [https://doi.org/10.1007/978-3-319-44680-6\\_2](https://doi.org/10.1007/978-3-319-44680-6_2).
- [70] S. Vijay, H.H. Kristoffersen, Y. Katayama, Y. Shao-Horn, I. Chorkendorff, B. Seger, K. Chan, How to extract adsorption energies, adsorbate–adsorbate interaction parameters, and saturation coverages from temperature programmed desorption experiments, *PCCP* 23 (40) (2021) 23346–23358, <https://doi.org/10.1039/D1CP03237B>.
- [71] L.M. Anovitz, D.R. Cole, Characterization and analysis of porosity and pore structures, *Rev. Min. Geochem.* 80 (1) (2015) 61–164, <https://doi.org/10.2138/rmg.2015.80.04>.
- [72] W. Zhang, A. Mehrabian, Coupled poromechanics and adsorption in multiple-porosity solids, *Phys. Solid State* 26 (5) (2023) 402–414, <https://doi.org/10.1134/S102959923040033>.
- [73] T. Yamashita, Molecular dynamics simulation for investigating antigen–antibody interaction, in: K. Tsumoto, D. Kuroda (Eds.), *Computer-Aided Antibody Design*, vol. 2552, Humana, 2023, pp. 49–65, [https://doi.org/10.1007/978-1-0716-2609-2\\_4](https://doi.org/10.1007/978-1-0716-2609-2_4).
- [74] E. Akkus, O. Tayfuroglu, M. Yıldız, A. Kocak, Accurate binding free energy method from end-state MD simulations, *J. Chem. Inf. Model.* 62 (17) (2022) 4095–4106, <https://doi.org/10.1021/acs.jcim.2c00601>.
- [75] A. Torres-Knoop, A. Pouraeiadesfahani, T.J.H. Vlugt, D. Dubbeldam, Behavior of the enthalpy of adsorption in nanoporous materials close to saturation conditions, *J. Chem. Theory Comput.* 13 (7) (2017) 3326–3339, <https://doi.org/10.1021/acs.jctc.6b01193>.
- [76] Z. Taheri, A. Nakhaei Pour, Studying of the adsorption and diffusion behaviors of methane on graphene oxide by molecular dynamics simulation, *J. Mol. Model.* 27 (59) (2021), <https://doi.org/10.1007/s00894-021-04692-6>.
- [77] Z. Ahrestani, S. Sadeghzadeh, B.M. Emrooz, H., An overview of atmospheric water harvesting methods, the inevitable path of the future in water supply, *RSC Adv.* 15 (2023). <https://pubs.rsc.org/en/content/articlelanding/2023/ra/d2ra07733g>.
- [78] W. Xu, O.M. Yaghi, Metal–organic frameworks for water harvesting from air, anywhere, anytime, *ACS Central Sci.* 6 (8) (2020), <https://doi.org/10.1021/acscentsci.0c00848>.
- [79] M. Zhu, G. He, Z. Wang, J. Chen, X. Fu, H. Yang, P. Lyu, S. Gu, X. Liu, B. Shang, MOF-801 enabled rapid-cycling atmospheric water harvester with vertically aligned photothermal channel, *J. Environ. Chem. Eng.* 12 (5) (2024) 113815, <https://doi.org/10.1016/j.jece.2024.113815>.